# Global Air–Sea $CO_2$ Flux in 22 CMIP5 Models: Multiyear Mean and Interannual Variability*

FANG DONG

*Ministry of Education Key Laboratory for Earth System Modeling, Center for Earth System Science,
and School of Environment, Tsinghua University, Beijing, China*

YANGCHUN LI

*State Key Laboratory of Atmospheric Boundary Layer Physics and Atmospheric Chemistry,
Institute of Atmospheric Physics, Chinese Academy of Sciences, Beijing, China*

BIN WANG

*Ministry of Education Key Laboratory for Earth System Modeling, and Center for Earth
System Science, Tsinghua University, and State Key Laboratory of Numerical
Modeling for Atmospheric Sciences and Geophysical Fluid Dynamics, Institute of
Atmospheric Physics, Chinese Academy of Science, Beijing, China*

WENYU HUANG, YANYAN SHI, AND WENHAO DONG

*Ministry of Education Key Laboratory for Earth System Modeling, and Center for Earth System Science,
Tsinghua University, Beijing, China*

(Manuscript received 18 November 2014, in final form 12 January 2016)

ABSTRACT

To assess the capability of the latest Earth system models (ESMs) in representing historical global air–sea $CO_2$ flux, 22 models from phase 5 of the Coupled Model Intercomparision Project (CMIP5) are analyzed, with a focus on the spatial distribution of multiyear mean and interannual variability. Results show that the global distribution of air–sea $CO_2$ flux is reasonable in most of the models and that the main differences between models and observationally based results exist in regions with strong vertical movement. The annual mean flux in the 18-member multimodel ensemble (MME; four models were excluded because of their poor performances) mean during 1996–2004 is $1.95 \, \mathrm{Pg} \, \mathrm{C} \, \mathrm{yr}^{-1}$ ($1 \, \mathrm{Pg} = 10^{15} \, \mathrm{g}$; positive values mean into the ocean), and all but one model describe the rapid increasing trend of air–sea $CO_2$ flux observed during 1960–2000. The first mode of the global air–sea $CO_2$ flux variability during 1870–2000 in six of the models represents the El Niño–Southern Oscillation (ENSO) mode. The remaining 12 models fail to represent this important character for the following reasons: in five models, the tropical Pacific does not play a dominant role in the interannual variability of global air–sea $CO_2$ flux because of stronger interannual variability in the Southern Ocean; two models poorly represent the interannual fluctuation of dissolved inorganic carbon (DIC) in the surface ocean of the tropical Pacific; and four models have shorter periods of the air–sea $CO_2$ flux, which are out of the period range of ENSO events.

## 1. Introduction

The ocean plays key roles in regulating atmospheric $CO_2$ concentration and affecting climate change (Sabine et al. 2004; Le Quéré et al. 2009, 2010; Doney et al. 2014). The ocean had taken 48% of the total anthropogenic $CO_2$ emissions during 1800–1994 based on direct measurements of inorganic carbon (Sabine et al.

2004) and had taken about 33% of the total anthropogenic $CO_2$ emissions during 1960–2007 based on models forced by observed atmospheric $CO_2$ (Sarmiento et al. 2010). There exists a large uncertainty in these estimates, however, which results from both the differences among various approaches (e.g., approaches based on observations, inversion models, and forward models) and the accuracies of these approaches (e.g., sparse observational data coverage and uncertainty in model parameterizations) (Gruber et al. 2009; Wanninkhof et al. 2013).

Air–sea $CO_2$ flux can directly indicate the ocean's ability for $CO_2$ uptake. The flux can be obtained from both observationally based estimates and model outputs. The estimations based on observations shared similar characteristics with air–sea $CO_2$ flux (Takahashi et al. 1997, 2002, 2009; Feely et al. 2002, 2006; McNeil et al. 2007), although large differences were induced by the differences among various methods for estimating air–sea $CO_2$ flux based on observations. For example, the global air–sea $CO_2$ flux for 1995 estimated by observationally based methods is within the range from $1.8 \pm 0.5$ (Sweeney et al. 2007) to $2.2 \pm 0.4 \, Pg \, C \, yr^{-1}$ ($1 \, Pg = 10^{15} \, g$; Feely et al. 2001; Mikaloff Fletcher et al. 2006). Even when using the same method, uncertainty can be large because of the inadequacy of observational data in time and space and the different parameterization schemes used in each method (Boutin and Etcheto 1997; Gloor et al. 2003; Key et al. 2004; Xu et al. 2005; Le Quéré et al. 2010; Sasse et al. 2013).

Model outputs can make up for the temporal–spatial limitation in observations to some extent. Many researchers have estimated the air–sea $CO_2$ flux based on model outputs and applied the carbon cycle models for future climate change projection (Sarmiento et al. 2000; Jones et al. 2001; Orr et al. 2001; Wetzel et al. 2005; Friedlingstein et al. 2006; Bao et al. 2012; Dufresne et al. 2013; Giorgetta et al. 2013; Romanou et al. 2013; Ishii et al. 2014). It should be noted that the differences between models and the differences between models and observations are quite large. For example, the global oceanic anthropogenic $CO_2$ uptake in different approaches and model outputs for the periods of the 1990s and the early 2000s ranges from 1.9 to $2.4 \, Pg \, C \, yr^{-1}$, and the uncertainty ranges from $\pm 0.2$ to $\pm 0.6 \, Pg \, C \, yr^{-1}$ (Gruber et al. 2009; Frölicher et al. 2015). The magnitudes of global air–sea $CO_2$ flux interannual variability in different methods are not consistent with each other; for example, they are $0.14 \, Pg \, C \, yr^{-1}$ for 1982–2007 [one standard deviation ($1\sigma$); Park et al. 2010], $0.28 \, Pg \, C \, yr^{-1}$ for 1980–98 [root-mean-square error (RMSE); McKinley et al. 2004b], and $0.40 \, Pg \, C \, yr^{-1}$ for 1979–97 ($1\sigma$; Le Quéré et al. 2000). Many ocean models showed good skills at representing spatial distribution features and interannual variability of the air–sea $CO_2$ flux (Le Quéré et al. 2000, 2010; Obata and Kitamura 2003; McKinley et al. 2004a,b; Patra et al. 2005; Doney et al. 2009; Li and Xu 2013; Wanninkhof et al. 2013), but how well do the current Earth system models (ESMs) work in terms of simulating air–sea $CO_2$ flux when the ocean carbon cycle and climate change are coupled? The answer to the question will help us judge whether or not their future projections are reliable. Although we cannot verify these future projections right now, we can validate these models' performances in terms of their simulations of the past.

The ESMs are essential tools for studying climate change, by which the ocean carbon cycle and climate can be fully coupled. Models from phase 5 of the Coupled Model Intercomparison Project (CMIP5) include the latest ESMs, which provide valuable scientific references for the Intergovernmental Panel on Climate Change Fifth Assessment Report (IPCC AR5). The ocean biogeochemistry component is included in most CMIP5 models for the first time in CMIP history (Taylor et al. 2012). The historical experiments by the CMIP5 models aimed at modeling the historical climate under the influences of natural and anthropogenic forcing derived from observations (Taylor et al. 2012). Assessment of CMIP5 models' abilities to simulate historical air–sea $CO_2$ flux is important, not only for reliable future prediction but also for further model development. Anav et al. (2013) examined the air–sea $CO_2$ flux simulated by CMIP5 models in terms of net flux in different latitude bands and seasonal changes. They proposed a method to access CMIP5 models' basic performances in simulating the mean state of air–sea $CO_2$ flux according to RMSE and probability density function. Frölicher et al. (2015) compared the similarity of air–sea $CO_2$ flux patterns simulated by CMIP5 models with the observationally based results of Landschützer et al. (2014) to investigate the Southern Ocean's dominant role in anthropogenic carbon uptake (and heat uptake). To have reliable projection of the air–sea $CO_2$ flux, it is important that these models not only capture the annual mean flux but also the interannual variability of the flux (Lenton et al. 2013). The interannual variation of air–sea $CO_2$ flux, which influences the atmospheric $CO_2$ concentration, can represent the interaction between carbon cycle and climate change to some extent. Such interaction is the key for climate change study, and interannual variation of air–sea $CO_2$ flux can represent the influence of climate change on the ocean carbon cycle. Based on these reasons, it is also necessary to evaluate simulations of air–sea $CO_2$ flux variability in CMIP5 models besides the annual mean flux. On the basis of these published studies, our objectives are as follows: 1) to characterize the spatial distribution biases of the multiyear mean of air–sea $CO_2$ flux and possible underlying causes for the biases; 2) to characterize the reliability of simulated

global air–sea $CO_2$ flux variation in the contemporary time period; and 3) to examine the interannual variability of simulated air–sea $CO_2$ flux in the tropical Pacific and possible causes underlying the biases in interannual variability.

We choose 22 CMIP5 models for evaluating their capabilities in simulating the historical air–sea $CO_2$ flux, which is forced by the historical atmospheric $CO_2$ concentration data. First, we compare the CMIP5 model results against the observationally based results of Valsala and Maksyutov (2010) from 1996 to 2004, including model biases in spatial distribution of air–sea $CO_2$ flux in the contemporary time period, and analyze the annual increasing trend of modeled air–sea $CO_2$ flux over a longer time (1870–2000). The analysis on the annual mean state provides a base for interannual variability analysis. Then we assess the simulated interannual variability from 1982–2005 using the diagnostic model results of Park et al. (2010). Finally, to avoid extreme events, we use the CMIP5 model outputs during a longer period (from 1870 to 2000) to conduct analysis on the possible causes for the unreasonable interannual variability of the air–sea $CO_2$ flux. The paper is organized as follows. We briefly introduce the validation data, models, and analysis methods in section 2. The main results are presented in sections 3 and 4. A summary and discussion are provided in section 5.

## 2. Datasets, models, and methodology

We use two sets of air–sea $CO_2$ flux data to validate the air–sea $CO_2$ flux in the CMIP5 models. One dataset is from Park et al. (2010, hereafter P2010), which extrapolated seasonal relationship between sea surface temperature (SST) and the partial pressure of $CO_2$ ($pCO_2$) to the interannual time scale. The other dataset is from Valsala and Maksyutov (2010, hereafter VM2010), which used multiyear individual observations of $pCO_2$ from Takahashi et al. (2007) as a constraint in a process model to resolve valuable information regarding the interannual variability of air–sea $CO_2$ flux and obtained an assimilated air–sea $CO_2$ flux estimate on a $1° \times 1°$ grid. The results from the two sets of data are referred to as observationally based results for brevity. The climatological regional patterns from the two sets of data compare well with each other for the period of 1996–2004 (Fig. S1 in the supplemental material; positive values for flux into the ocean). We choose to use the air–sea $CO_2$ flux from 1996–2004 in VM2010 to examine CMIP5 models' performances in simulating the mean state of air–sea $CO_2$ flux, with a focus on spatial distribution and amplitude. P2010 is used to validate interannual variability in these models over a slightly longer time period from 1982 to 2005. In this paper, one standard deviation (SD) of air–sea $CO_2$ flux anomalies (after the flux is

detrended and deseasoned) is used to indicate the magnitude of variability. The observational data of SST used in the analysis come from the Hadley Centre Sea Ice and Sea Surface Temperature dataset (HadISST; Rayner et al. 2003), which has $1° \times 1°$ resolution from 1870 to date. HadISST temperatures are reconstructed using a two-stage reduced-space optimal interpolation procedure, followed by superposition of quality-improved gridded observations onto the reconstructions to restore local detail (the detailed description of the dataset and its production process can be found at http://www.metoffice. gov.uk/hadobs/hadisst/data/download.html). This dataset has been used broadly and is considered reliable (Hurrell et al. 2008; Maksyutov et al. 2012; Anav et al. 2013; Wanninkhof et al. 2013). The observational data of net primary production by all kinds of phytoplankton (intpp) come from satellite product of SeaWiFS (ftp://ftp.icess. ucsb.edu/pub/org/oceancolor/MEaSUREs/NPP/8day/ VGPM/Seawifs/). It can represent the effect of biological pump in $CO_2$ uptake to some extent (Lutz et al. 2007).

The outputs of 22 ESMs in the CMIP5 (Table 1) are obtained through data portals of the Earth System Grid Federation (http://pcmdi9.llnl.gov/). A total of 23 models provide outputs of air–sea $CO_2$ flux. Among them, the Beijing Climate Center provided two versions of one model, and we choose the more frequently used version. The outputs of the historical experiments (r1i1p1) for the twentieth century are used in this study, including monthly air–sea $CO_2$ flux (for all 22 models), sea surface dissolved inorganic carbon (DIC; available for 17 of the 22 models), intpp (available for 18 of the 22 models), maximum mixed layer depth (MLD; available for 11 out of the 22 models, but we could only access the outputs of nine models at present), and SST (for all 22 models). Note that the air–sea $CO_2$ flux from BNU-ESM and CanESM2 was expressed as $CO_2$ instead of carbon, so the air–sea $CO_2$ flux of these two models was multiplied by 12/44 to convert it from $CO_2$ to C units.

Because of different resolutions used in these models, the CMIP5 outputs are regridded to the same $1° \times 1°$ first. To evaluate the overall performance in simulating air–sea $CO_2$ flux, centered spatial correlation coefficient (SCC) and RMSE are calculated with respect to the observationally based results of VM2010. Empirical orthogonal function (EOF) decomposition, power spectral analysis, and correlation analysis are employed to analyze the interannual variability of air–sea $CO_2$ flux. The outputs are all detrended by the least squares method, and the annual cycle is removed before applying EOF decomposition and calculating anomalies. To analyze the relation between air–sea $CO_2$ flux and SST, the correlation coefficient (CC) between their principal components of the first mode in EOF (PC1) is calculated in different

TABLE 1. CMIP5 models used in this study. (Many acronym expansions are available at http://www.ametsoc.org/PubsAcronymList.)

| Model | Country and research center | Ocean model component | Ocean biogeochemistry component | Ocean resolution (lat × lon, levels) |
|---|---|---|---|---|
| BCC_CSM1.1 | China, BCC | MOM,version 4 with 40 levels (MOM4-L40) | Carbon mode of Ocean Carbon Cycle Model Intercomparison Project phase 2 (OCMIP2) | (0.3–1)° × 1.0°, L40 |
| BNU-ESM | China, Beijing Normal University (BNU) | MOM4.1 | Idealized ocean biogeochemistry (iBGC) | 0.9° × 1.0°, L50 |
| CanESM2 | Canada, CCCma | Fourth Generation Canadian Ocean Model (CanOM4) | CMOC | 0.9° × 1.4°, L40 |
| CESM1 with biogeochemistry [CESM1(BGC)] | United States, National Science Foundation (NSF)–DOE–NCAR | POP, version 2 (POP2) | Biogeochemical Elemental Cycling (BEC) | 320 × 384 points (gx1v3), L60 |
| CMCC-CESM | Italy, CMCC | OPA, version 8.2 (OPA8.2) | Pelagic Biogeochemistry for Global Ocean Simulations (PELAGOS) | 2.0° average, 0.5° at the equator (ORCA2 grid) |
| CNRM-CM5 | France, CNRM–Centre Européen de Recherche et de Formation Avancée en Calcul Scientifique (CERFACS) | NEMO, version 3.2 (NEMOv3.2) | Pelagic Interaction Scheme for Carbon and Ecosystem Studies (PISCES) | 0.7° × 0.7°, L42 |
| GFDL-ESM2G | United States, NOAA/GFDL | GOLD | Tracers in the Ocean with Allometric Zooplankton, version 2 (TOPAZ2) | 0.6° × 1.0° (tripolar), L63 |
| GFDL-ESM2M | United States, NOAA/GFDL | MOM4.1 | TOPAZ2 | 0.6° × 1.0° (tripolar), L50 |
| GISS-E2-H-CC | United States, NASA GISS | HYCOM | NASA Ocean Biogeochemical Model (NOBM) | (1–0.2)° × 1°, L26 |
| GISS-E2-R-CC | United States, NASA GISS | Russell ocean model | NOBM | 1° × 1.25°, L32 |
| HadGEM2-CC | United Kingdom, Met Office Hadley Centre (MOHC) | HadGEM2-CC ocean component | Diatoms and Other Phytoplankton within Hadley Centre Ocean Carbon Cycle (Diat-HadOCC) | (0.3–1)° × 1°, L40 |
| HadGEM2-ES | United Kingdom, MOHC | HadGEM2-ES ocean component | Diat-HadOCC | (0.3–1)° × 1°, L40 |
| INM-CM4.0 | Russia, INM | INM-CM4.0 ocean component | Simple model into INM-CM4.0 ocean component | 0.5° × 1.0°, L40 |
| IPSL-CM5A-LR | France, IPSL | NEMO | PISCES | 2° × 2°, L31 |
| IPSL-CM5A-MR | France, IPSL | NEMO | PISCES | 2° × 2°, L31 |
| IPSL-CM5B-LR | France, IPSL | NEMO | PISCES | 2° × 2°, L31 |
| MIROC-ESM | Japan, JAMSTEC; Atmosphere and Ocean Research Institute (AORI); National Institute for Environmental Studies | COCO, version 3.4 (COCO3.4) | Nutrient–Phytoplankton–Zooplankton–Detritus (NPZD) | 0.9° × 1.4°, L44 |
| MIROC-ESM-CHEM | Japan, JAMSTEC; AORI; National Institute for Environmental Studies | COCO3.4 | NPZD | 0.9° × 1.4°, L44 |

TABLE 1. (*Continued*)

| Model | Country and research center | Ocean model component | Ocean biogeochemistry component | Ocean resolution (lat × lon, levels) |
|---|---|---|---|---|
| MPI-ESM-LR | Germany, Max Planck Institute for Meteorology (MPI-M) | MPI-OM | Fifth Hamburg Model of the Ocean Carbon Cycle (HAMOCC5) | 1.5° × 1.5°, L40 |
| MPI-ESM-MR | Germany, MPI-M | MPI-OM | HAMOCC5 | 0.4° × 0.4°, L40 |
| MRI-ESM1 | Japan, MRI | Meteorological Research Institute Community Ocean Model, version 3 (MRI.COM-3) | NPZD | 0.5° × 1°, L51 |
| NorESM1-ME | Norway, Norwegian Climate Centre (NCC) | Miami Isopycnic Coordinate Ocean Model (MICOM) | HAMOCC5 | 0.5° × 1°, L53 |

regions when the spatial patterns of their first modes in EOF (EOF1) are similar.

## 3. Multiyear mean of air–sea CO$_2$ flux in CMIP5 models

### a. Spatial distribution of model biases

Compared with observationally based results of VM2010, which is chosen as a reference for its high-resolution of 1° × 1° and good comparison with Takahashi et al. (2009), most of the CMIP5 models have similar simulated biases of 9-yr-averaged air–sea CO$_2$ flux from 1996 to 2004, mainly in the northwestern Pacific, the deep-water formation area of the North Atlantic, and the Southern Ocean south of 45°S (Fig. 1), which are also the main air–sea CO$_2$ exchange regions (Fig. S1) and where models differ among themselves most (Fig. 2).

Most models overestimate the uptake in the northwestern Pacific (Fig. 1), and seven models fail to reproduce the CO$_2$ source in the Bering Sea (Fig. S1), which is induced by winter convection (Takahashi et al. 2002). The reasons for the failure in the Bering Sea are different in the seven models. As shown in Fig. S2 of the supplemental material, SSTs in BCC_CSM1.1, BNU-ESM, and NorESM1-ME are obviously colder than the observationally based SST in the Bering Sea, which increases the solubility of CO$_2$ and may offset the outgassing of CO$_2$ induced by winter convection. The SSTs in MIROC-ESM and MIROC-ESM-CHEM are warmer than the observationally based SST north of 30°N in the Pacific. The warmer SST may restrain the convection in winter. We are unable to figure out the reason for the overestimated CO$_2$ uptake in MRI-ESM1, because there is strong winter convection (Fig. S3 in the supplemental material) in the northwestern Pacific, which gives a warmer SST than the observationally based SST because of the temperature inversion below 100 m in winter, and the simulated intpp is lower than that of the satellite product (Fig. S4 in the supplemental material).

In the deep-water formation area of the North Atlantic, all models but BNU-ESM and INM-CM4.0 have a weaker CO$_2$ uptake. Comparison with the results of intpp based on the satellite product shows that most models have underestimated intpp (e.g., CanESM2, CNRM-CM5, GFDL-ESM2G/M, GISS-E2-H/R-CC, HadGEM2-CC/ES, IPSL-CM5B-LR, MPI-ESM-LR, and MRI-ESM1; Fig. S4). In addition, most models show a weaker Atlantic meridional overturning circulation (AMOC) associated with the colder SST in the Northern Hemisphere, including CanESM2, CNRM-CM5, GFDL-ESM2G/M, GISS-E2-H/R-CC, HadGEM2-CC/ES, IPSL-CM5B-LR, and MPI-ESM-LR, according to Wang et al. (2014). A weak AMOC would lead to increased stratification and
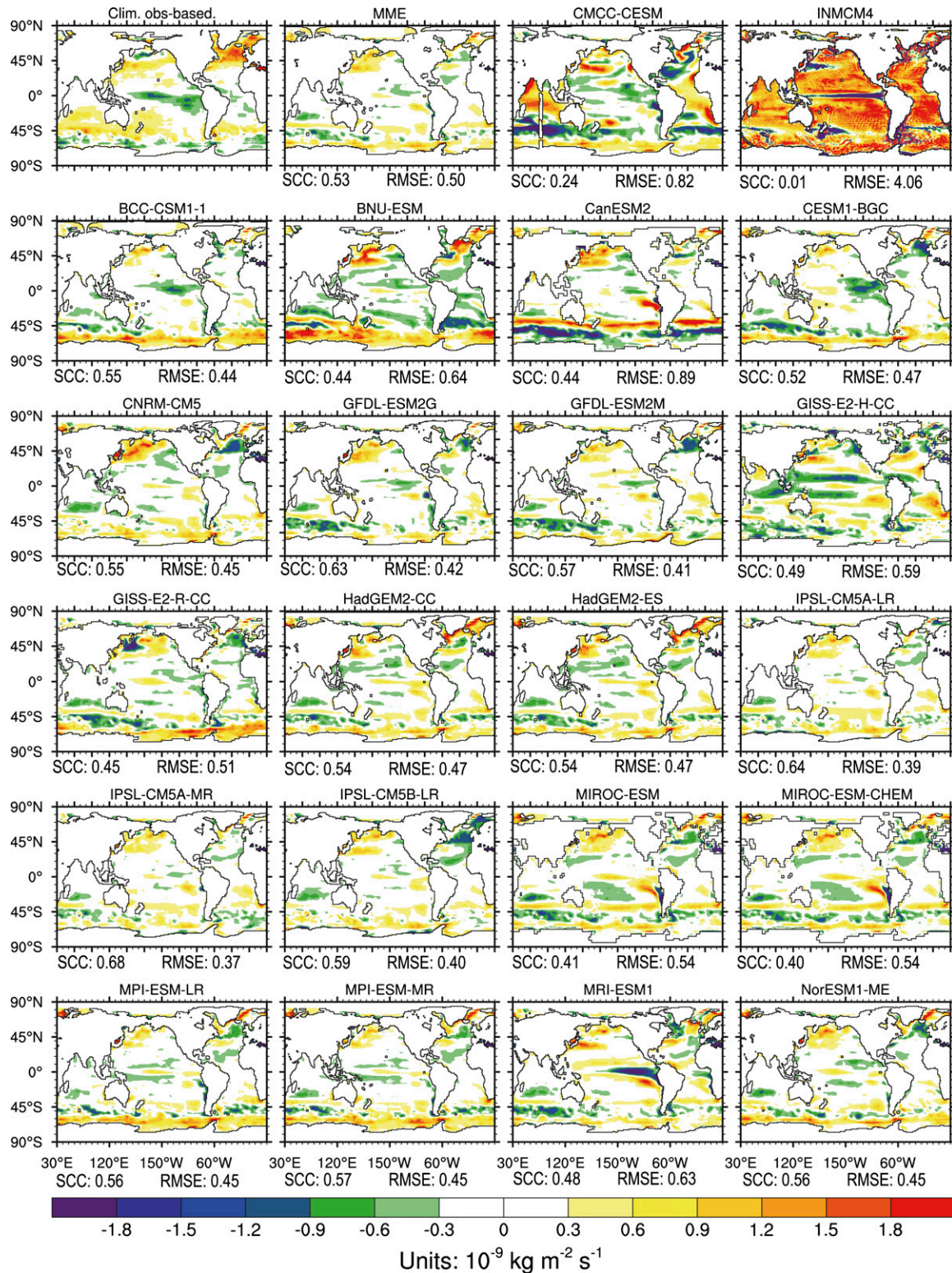
FIG. 1. The annual mean air–sea $CO_2$ flux ($10^{-9}$ kg m$^{-2}$ s$^{-1}$) during 1996–2004 (VM2010) and model biases with respect to the observationally based results of VM2010 (model results minus observationally based results). (top left) The air–sea $CO_2$ flux climatology from the observationally based results of VM2010. The model name is given at the top of each panel. MME is the MME mean of air–sea $CO_2$ flux of the 18 models. Positive value means the flux is into the ocean. The SCCs and RMSEs ($10^{-9}$ kg m$^{-2}$ s$^{-1}$) with respect to the observationally based results are given below each panel. Note that the two models CMCC-CESM and INM-CM4.0 with higher RMSEs and lower SCCs compared to the observationally based results, and the two models GISS-E2-H/R-CC with $CO_2$ outgassing from the ocean during 1870–2000 are excluded.
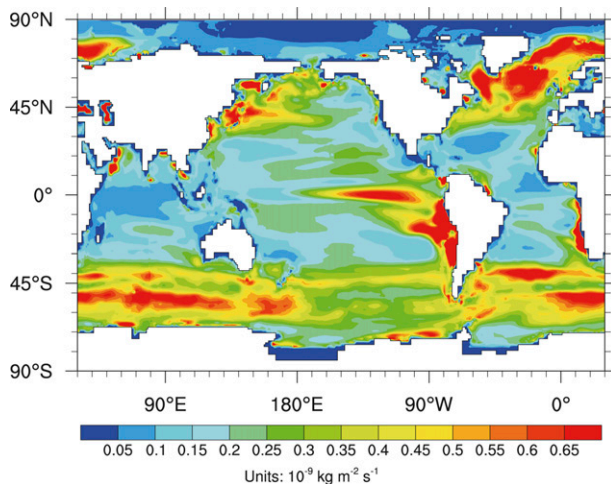
FIG. 2. One standard deviation of the air–sea $CO_2$ flux ($10^{-9}$ kg m$^{-2}$ s$^{-1}$) among 18 models (the four models CMCC-CESM, INM-CM4.0, and GISS-E2-H/R-CC are excluded), based on the annual mean air–sea $CO_2$ flux of the 18 models during 1996–2004. It indicates where models differ most in terms of air–sea $CO_2$ flux.

slower surface-to-deep-ocean transport of $CO_2$ (Maier-Reimer et al. 1996; Obata 2007; Zickfeld et al. 2008). A weaker AMOC can also affect the magnitude of biological pump in two ways (Maier-Reimer et al. 1996; Schmittner 2005): the increased stratification hampers nutrient transports from the deep ocean to the surface layer and increases the residence time of the nutrients at the sea surface. The interplay between the two determines the response of ocean biological activity to AMOC weakening. Underestimated intpp in models indicates a restrained role of the weaker AMOC in the biological pump of $CO_2$ uptake.

In the Southern Ocean, the models generally display weak $CO_2$ outgassing (e.g., the three models of IPSL) or carbon sinking in the open ocean around 60°S [e.g., BCC_CSM1.1, BNU-ESM, CMCC-CESM, CESM1 (BGC), and MPI-ESM-LR/MR]. Except for the two models CanESM2 and GISS-E2-R-CC, the distributions of the air–sea $CO_2$ flux in the other models do not agree with those in the observationally based results in the higher latitudes (south of 50°S) of the Southern Hemisphere. Morrison et al. (2015) indicated that the regions around 60°S still act as carbon sources for the atmosphere in the contemporary time period because of strong upwelling, which is consistent with the observationally based results of Takahashi et al. (2009) and VM2010. Previous studies showed that the behaviors of air–sea $CO_2$ exchange in the Southern Ocean are highly affected by water-mass formation and deep convection (Marinov et al. 2006; Crueger et al. 2008; Séférian et al. 2012), as well as upwelling (Morrison et al. 2015) and

biological activities (Marinov et al. 2006). The biases in the bottom-water formation region of the Southern Ocean reported in Heuzé et al. (2013) imply that most CMIP5 models simulated much stronger (unrealistically extensive) deep convection in the open ocean of the Southern Ocean. Such unrealistic deep convection in the models strengthens water-mass formation in the ocean. Wang et al. (2014) also showed a strengthening of the bottom-water formation in the Southern Ocean under the condition of reduced AMOC. The strengthening of bottom-water formation may reduce $CO_2$ outgassing around 60°S to some extent, which is reduced by the convection in the upper ocean. However, the much weaker outgassing or the carbon sink around 60°S in the models also stems from the overestimated intpp in the high latitudes of the Southern Ocean [e.g., CESM1(BGC), CNRM-CM5, GFDL-ESM2G/M, GISS-E2-H/R-CC, HadGEM2-CC/ES, MPI-ESM-LR/MR, and NorESM1-ME; see Fig. S4]. The roles of stronger bottom-water formation and intpp even exceed the promotion of upwelling and simulated warmer SST (Fig. S2) for $CO_2$ outgassing. In this case, the reduction of Antarctic sea ice extent (SIE) (Turner et al. 2013) would favor more $CO_2$ uptake around 60°S in the CMIP5 models.

The SCC and RMSE of each model with respect to the results of VM2010 show that most of the models perform well in terms of global annual mean flux of air–sea $CO_2$ (SCC larger than 0.50 and RMSE smaller than 0.50 × $10^{-9}$ kg m$^{-2}$ s$^{-1}$; Fig. 1). The SCCs in the two models (CMCC-CESM and INM-CM4.0) with bigger biases are 0.24 and 0.01, respectively, and the SCCs in the other 20 models are between 0.40 and 0.68. The RMSEs in the three models CanESM2, CMCC-CESM and INM-CM4.0 are 0.89, 0.82, and 4.06 × $10^{-9}$ kg m$^{-2}$ s$^{-1}$, respectively, and those in the other 19 models are between 0.37 and 0.64 × $10^{-9}$ kg m$^{-2}$ s$^{-1}$. Excluding CMCC-CESM and INM-CM4.0 for their low SCCs and high RMSEs, and excluding GISS-E2-H/R-CC for their negative total net air–sea $CO_2$ flux from 1850 to 2000, only 18 models are used for multimodel ensemble (MME) mean and interannual variation analysis. The MME mean SCC and RMSE of the 18 models are 0.53 and 0.49 × $10^{-9}$ kg m$^{-2}$ s$^{-1}$, respectively. Of the 18 models, 12 models have higher SCCs and smaller RMSEs compared with the MME mean; they are BCC_CSM1.1, CNRM-CM5, GFDL-ESM2G/M, HadGEM2-CC/ES, IPSL-CM5A-LR/MR, IPSL-CM5B-LR, MPI-ESM-LR/MR, and NorESM1-ME. The global annual mean flux of the 18 CMIP5 models during 1996–2004 is 1.95 Pg C yr$^{-1}$. This value is similar to the estimate of Patra et al. (2005), which is 1.88 Pg C yr$^{-1}$ during the 1990s based on an atmospheric inverse model, and is in the range of

TABLE 2. Annual mean flux and annual mean increment of air–sea $CO_2$ flux during 1870–1959 and 1960–2000 in 22 CMIP5 models.

| Models | 1870–1959 | | 1960–2000 | |
| --- | --- | --- | --- | --- |
| | Annual mean flux (Pg C yr$^{-1}$) | Annual mean increments (Pg C yr$^{-2}$) | Annual mean flux (Pg C yr$^{-1}$) | Annual mean increments (Pg C yr$^{-2}$) |
| BCC_CSM1.1 | 0.44 | 0.0005 ($R^2 = 0.3728$) | 1.39 | 0.0298 ($R^2 = 0.927$) |
| BNU-ESM | 0.48 | 0.0032 ($R^2 = 0.2315$) | 1.29 | 0.0227 ($R^2 = 0.7979$) |
| CanESM2 | 0.43 | 0.0026 ($R^2 = 0.0966$) | 1.31 | 0.0236 ($R^2 = 0.8099$) |
| CESM1(BGC) | 0.37 | 0.0038 ($R^2 = 0.2385$) | 1.31 | 0.028 51 ($R^2 = 0.8626$) |
| CMCC-CESM | 0.22 | 0.0084 ($R^2 = 0.2596$) | 1.49 | −0.0031 ($R^2 = 0.0084$) |
| CNRM-CM5 | 0.48 | 0.0039 ($R^2 = 0.3001$) | 1.27 | 0.0333 ($R^2 = 0.8719$) |
| GFDL-ESM2G | 0.30 | 0.0050 ($R^2 = 0.3598$) | 1.29 | 0.0306 ($R^2 = 0.8498$) |
| GFDL-ESM2M | 0.35 | 0.0058 ($R^2 = 0.3097$) | 1.39 | 0.0347 ($R^2 = 0.7237$) |
| GISS-E2-H-CC | −0.61 | 0.0045 ($R^2 = 0.2963$) | 0.44 | 0.0299 ($R^2 = 0.8836$) |
| GISS-E2-R-CC | −0.33 | 0.0058 ($R^2 = 0.3352$) | 0.78 | 0.0334 ($R^2 = 0.8074$) |
| HadGEM2-CC | 0.48 | 0.0051 ($R^2 = 0.5407$) | 1.52 | 0.0294 ($R^2 = 0.9024$) |
| HadGEM2-ES | 0.45 | 0.0049 ($R^2 = 0.4775$) | 1.52 | 0.031 ($R^2 = 0.9329$) |
| INM-CM4.0 | 3.71 | 0.0049 ($R^2 = 0.0745$) | 4.82 | 0.0361 ($R^2 = 0.7097$) |
| IPSL-CM5A-LR | 0.69 | 0.0049 ($R^2 = 0.4203$) | 1.57 | 0.0261 ($R^2 = 0.9072$) |
| IPSL-CM5A-MR | 0.48 | 0.0060 ($R^2 = 0.4962$) | 1.49 | 0.0351 ($R^2 = 0.8749$) |
| IPSL-CM5B-LR | 0.36 | 0.0045 ($R^2 = 0.4899$) | 1.24 | 0.0267 ($R^2 = 0.9521$) |
| MIROC-ESM | 0.44 | 0.0043 ($R^2 = 0.3081$) | 1.44 | 0.0343 ($R^2 = 0.9018$) |
| MIROC-ESM-CHEM | 0.42 | 0.0036 ($R^2 = 0.2552$) | 1.42 | 0.0309 ($R^2 = 0.8967$) |
| MPI-ESM-LR | 0.44 | 0.0045 ($R^2 = 0.4543$) | 1.41 | 0.0334 ($R^2 = 0.8723$) |
| MPI-ESM-MR | 0.46 | 0.0034 ($R^2 = 0.1953$) | 1.43 | 0.0297 ($R^2 = 0.8415$) |
| MRI-ESM1 | 0.39 | 0.0046 ($R^2 = 0.3549$) | 1.41 | 0.0328 ($R^2 = 0.9270$) |
| NorESM1-ME | 0.64 | 0.0048 ($R^2 = 0.5435$) | 1.73 | 0.0329 ($R^2 = 0.9416$) |
| MME (18 models) | 0.45 ± 0.09 | 0.0042 ± 0.0013 | 1.43 ± 0.24 | 0.0304 ± 0.0022 |

1.5–2.0 Pg C yr$^{-1}$ for the 1990s obtained by some earlier studies (Battle et al. 2000; Takahashi et al. 2002; Gloor et al. 2003).

### b. Annual mean $CO_2$ uptake by the ocean and its evolution

Here, we combine the annual mean and the annual increasing trend of air–sea $CO_2$ flux during 1870–2000 (a much longer time period to avoid the influence of extreme values in a short time period), to reveal the important ocean zones for $CO_2$ uptake. The annual increasing trend of air–sea $CO_2$ flux is obtained by linear regression analysis using the least squares method. The global air–sea $CO_2$ flux in the 18 CMIP5 models (excluding CMCC-CESM and INM-CM4.0 for their low SCCs and high RMSEs, and excluding GISS-E2-H/R-CC for their negative total net air–sea $CO_2$ flux from 1850 to 2000) increased slowly before 1960 and increased rapidly during 1960–2000 [Fig. 13 in Anav et al. (2013); Table 2]. Table 2 shows that most models had no obvious increase during 1870–1959; for example, the annual increments were between 0.0005 and 0.0051 Pg C yr$^{-1}$, with $R^2$ ranging between 0.0966 and 0.5435 (Table 2). Over the period of 1960–2000, the observationally based atmospheric $CO_2$ increased rapidly, which might have caused a rapid increase of global air–sea $CO_2$ flux. Therefore, we mainly analyze the trends during 1960–2000 next. The global annual mean air–sea $CO_2$ flux in CMCC-CESM increased rapidly during 1959–63 for an unknown reason, with a flux of 2.47 Pg C yr$^{-1}$ in 1963 and reducing in the following several years, which results in a different increasing trend from the other models (Fig. 3). The two models GISS-E2-H/R-CC had strong $CO_2$ outgassing from the ocean in 1870 and then $CO_2$ uptake until the year of 1960 (Fig. 3). The $CO_2$ outgassing in GISS-E2-H/R-CC during 1870–1960 was different from the other models; so was the overall large uptake in INM-CM4.0. During 1960–2000, the annual increase at the global scale (Table 2) was in the range of 0.0227–0.0351 Pg C yr$^{-1}$ ($R^2$ in the range of 0.7097–0.9521) for the 18 models.

In the scale of the two hemispheres, most of the CMIP5 models show that the Southern Hemisphere had a more rapid increasing rate from 1960–2000, while the Northern Hemisphere had a slower increasing rate (Fig. 3). In terms of MME mean of the 18 models, the annual mean air–sea $CO_2$ flux over 15°–90°S (0.95 Pg C yr$^{-1}$) is slightly smaller than that over 15°–90°N (1.11 Pg C yr$^{-1}$), but the annual mean increasing rate over 15°–90°S (0.016 Pg C yr$^{-2}$; $R^2 = 0.9724$) is twice that over 15°–90°N (0.008 Pg C yr$^{-2}$; $R^2 = 0.9309$).

For the region south of 15°S in the Southern Hemisphere, the main uptake is between 15° and 50°S, with an annual mean air–sea $CO_2$ flux of 0.89 Pg C yr$^{-1}$ and an
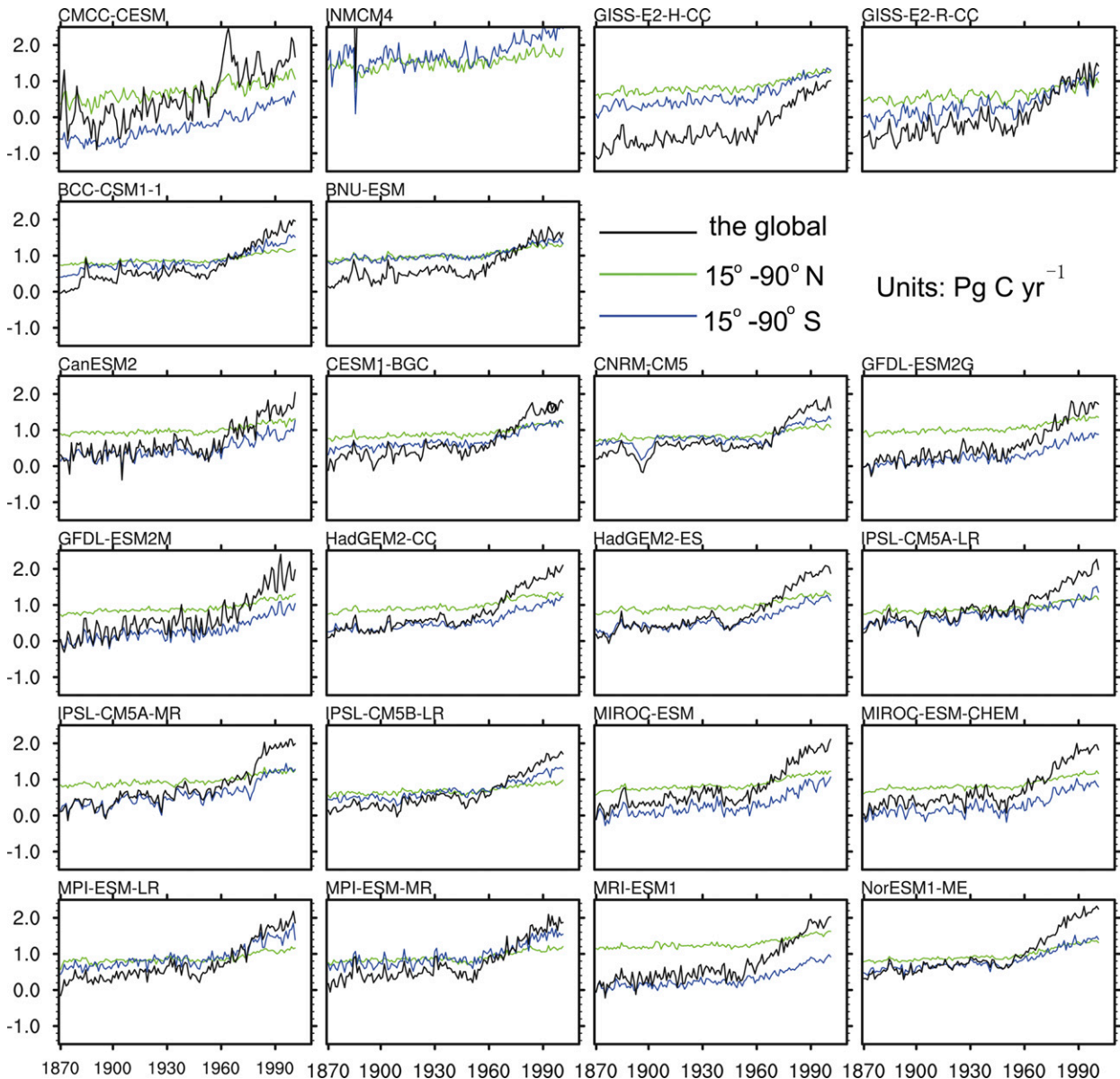
FIG. 3. The annual mean air–sea $CO_2$ flux (Pg C yr$^{-1}$) during 1870–2000. Curves represent the global (black), 15°–90°N (green), and 15°–90°S (blue).

annual mean increasing rate of 0.009 Pg C yr$^{-2}$ ($R^2 = 0.9504$). The region between 50°–90°S is a weak uptake area (0.06 Pg C yr$^{-1}$), but with an annual mean increasing rate of 0.007 Pg C yr$^{-2}$ ($R^2 = 0.9484$), which is close to the annual mean increasing rate over 15°–50°S. The larger increasing trend in the Southern Hemisphere may be associated with its dominating role in taking up anthropogenic $CO_2$ (Frölicher et al. 2015). Latest studies highlighted that the Southern Ocean had taken up a major fraction of anthropogenic carbon in the recent decades because of its deep-water upwelling (Morrison et al. 2015), which was also reported by earlier ocean modeling results (Li et al.

2012). In addition, the negative trend of the SIE during 1979–2005 in the CMIP5 models (Turner et al. 2013) would favor more anthropogenic $CO_2$ uptake by the ocean.

As a short summary, section 3 highlights that the CMIP5 models have biases mainly over the regions with strong vertical movement, where large differences also exist among the observationally based results, whereas most of the models perform well in terms of global annual mean flux of the air–sea $CO_2$ flux, and most of the models have good skills at representing the $CO_2$ uptake capacity in different regions except for the Southern Ocean. Different increasing rates of air–sea $CO_2$ flux in the two hemispheres
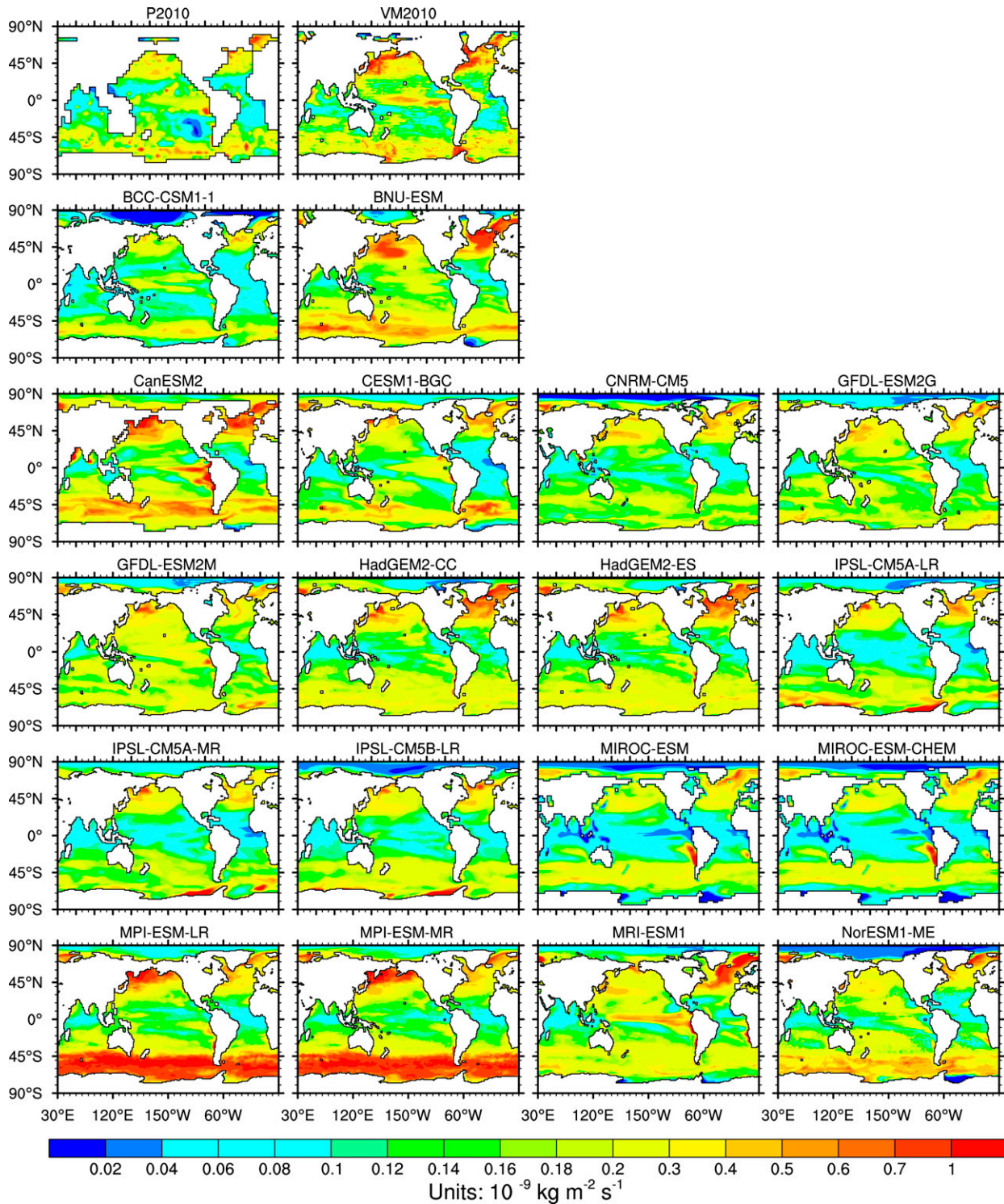
FIG. 4. Magnitude of air–sea $CO_2$ flux interannual variability ($10^{-9}$ kg m$^{-2}$ s$^{-1}$), which is expressed as one SD of the monthly air–sea $CO_2$ flux during 1982–2005 (except for VM2010 during 1996–2004 and HadGEM2-CC during 1982–2004). The fluxes are detrended and deseasoned first. To show the variation better, we use a nonlinear color scaling.

TABLE 3. Magnitude of air–sea $CO_2$ flux's interannual change (Pg C yr$^{-1}$) during 1982–2005, expressed as $1\sigma$ of the annual air–sea $CO_2$ flux anomalies.

| Models | Global | 15°–80°N | 45°–80°N | Tropical Pacific (15°S–15°N) | 15°–80°S | 45°–80°S |
|---|---|---|---|---|---|---|
| P2010 | 0.14 | 0.04 | 0.03 | 0.07 | 0.06 | 0.05 |
| BCC_CSM1.1 | 0.11 | 0.03 | 0.02 | 0.06 | 0.08 | 0.07 |
| BNU-ESM | 0.15 | 0.05 | 0.04 | 0.07 | 0.06 | 0.07 |
| CanESM2 | 0.18 | 0.05 | 0.04 | 0.11 | 0.14 | 0.13 |
| CESM1(BGC) | 0.12 | 0.03 | 0.02 | 0.10 | 0.07 | 0.05 |
| CNRM-CM5 | 0.10 | 0.04 | 0.03 | 0.03 | 0.05 | 0.04 |
| GFDL-ESM2G | 0.15 | 0.04 | 0.02 | 0.07 | 0.08 | 0.06 |
| GFDL-ESM2M | 0.28 | 0.05 | 0.03 | 0.16 | 0.12 | 0.07 |
| HadGEM2-CC | 0.09 | 0.04 | 0.03 | 0.03 | 0.07 | 0.07 |
| HadGEM2-ES | 0.10 | 0.04 | 0.04 | 0.03 | 0.08 | 0.08 |
| IPSL-CM5A-LR | 0.11 | 0.04 | 0.02 | 0.03 | 0.11 | 0.10 |
| IPSL-CM5A-MR | 0.08 | 0.05 | 0.03 | 0.03 | 0.06 | 0.06 |
| IPSL-CM5B-LR | 0.08 | 0.04 | 0.02 | 0.03 | 0.07 | 0.06 |
| MIROC-ESM | 0.12 | 0.03 | 0.02 | 0.03 | 0.12 | 0.09 |
| MIROC-ESM-CHEM | 0.12 | 0.04 | 0.03 | 0.02 | 0.11 | 0.08 |
| MPI-ESM-LR | 0.10 | 0.04 | 0.02 | 0.05 | 0.07 | 0.08 |
| MPI-ESM-MR | 0.13 | 0.06 | 0.05 | 0.03 | 0.09 | 0.09 |
| MRI-ESM1 | 0.13 | 0.04 | 0.03 | 0.11 | 0.06 | 0.05 |
| NorESM1-ME | 0.10 | 0.03 | 0.02 | 0.05 | 0.09 | 0.06 |

illustrate that the region south of 50°S is the important region for $CO_2$ uptake after the Industrial Revolution.

## 4. Interannual variability of global air–sea $CO_2$ flux in CMIP5 models

### a. Interannual variability during 1982–2005

Observationally based studies have reached the consensus that strong interannual variability of air–sea $CO_2$ flux exists in the tropical Pacific (15°S–15°N, 109°E–77°W) and at high latitudes of both hemispheres (e.g., P2010; VM2010; Landschützer et al. 2014; Rödenbeck et al. 2014). However, because of differences in study area, method, and time scale, magnitudes of interannual variability shown in these studies are different. For example, the interannual variability of global air–sea $CO_2$ flux is 0.31 Pg C yr$^{-1}$ in Rödenbeck et al. (2014) based on $1\sigma$ during 1993–2008 and an observation-data-driven mixed layer scheme. It is 0.12 Pg C yr$^{-1}$ in Landschützer et al. (2014) based on $1\sigma$ during 1998–2011 and observational $p$CO$_2$. It is 0.14 Pg C yr$^{-1}$ in P2010, based on $1\sigma$ during 1982–2007 and their diagnostic model results. The interannual variability ($1\sigma$) of global air–sea $CO_2$ flux in most CMIP5 models is similar to those of P2010 and Landschützer et al. (2014), but it is smaller than the result of Rödenbeck et al. (2014). In addition, the interannual variability of global air–sea $CO_2$ flux in most CMIP5 models is smaller than those in uncoupled ocean models (Le Quéré et al. 2000; Obata and Kitamura 2003; McKinley et al. 2004b; Doney et al. 2009), which are between 0.2 and 0.4 Pg C yr$^{-1}$. The large uncertainty in the interannual variability indicates that

the mechanism behind the variability needs further investigation.

Despite large differences in the interannual variability, the observationally based and modeling studies mentioned above all highlighted the strong variation of air–sea $CO_2$ flux in the tropical Pacific, which is dominated by El Niño–Southern Oscillation (ENSO)–induced variability in upwelling of DIC-rich deep water (Keeling and Revelle 1985; Feely et al. 1997, 1999; Jones et al. 2001; Obata and Kitamura 2003; McKinley et al. 2004b; Patra et al. 2005; P2010; Landschützer et al. 2014; Rödenbeck et al. 2014). This is also true for the results of VM2010, which is based on data of high resolution (Fig. 4) and covers the time period of 1996–2004. We use the results of P2010 for comparison because it is based on data of a longer period. Most of the CMIP5 models show similar interannual variability in high-latitude regions with that in P2010, whereas, except for BCC_CSM1.1, CanESM2, CESM1(BGC), GFDL-ESM2G/M, and MRI-ESM1, the other 12 models fail to show obvious fluctuations in the tropical Pacific.

The SD values of air–sea $CO_2$ flux in different regions are listed in Table 3. Three models (HadGEM2-CC, IPSL-CM5A-MR, and IPSL-CM5B-LR) underestimate global interannual variability, with an SD value less than 30% of that given by P2010. For the models with similar global SD values as P2010, the SD values over the tropical Pacific (15°S–15°N, 109°E–77°W) are weak for most of them [except for BNU-ESM, CanESM2, CESM1(BGC), GFDL-ESM2G/M, and MRI-ESM1]. The values over the tropical Pacific in nine of the models (CNRM-CM5, HadGEM2-CC/ES,
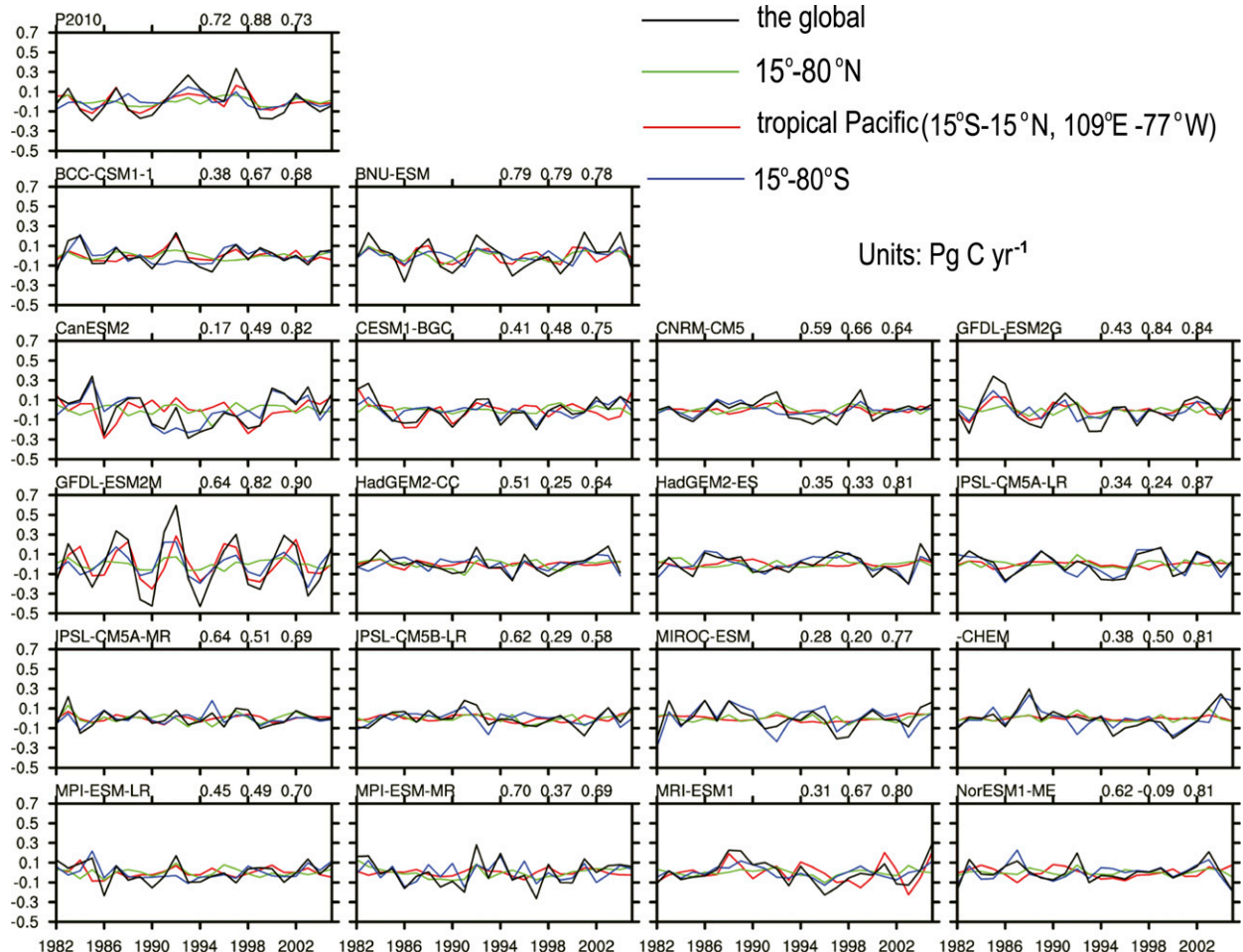
FIG. 5. Air–sea $CO_2$ flux anomalies (Pg C yr$^{-1}$) during 1982–2005 (except for HadGEM2-CC during 1982–2004). Curves represent the global (black), 15°–80°N (green), tropical Pacific (15°S–15°N, 109°E–77°W; red), and 15°–80°S (blue). Shown is (top left) the diagnostic model results of P2010; remaining panels are CMIP5 model results. The numbers at the top of each panel are the correlation coefficients between 15°–80°N and the global ocean, between the tropical Pacific and the global ocean, and between 15°–80°S and the global ocean. The anomalies are annual mean data and detrended first. When the sample size $n = 24$, the critical values of correlation coefficient at $\alpha = 0.05$ and $\alpha = 0.01$ are 0.40 and 0.52, respectively. When $n = 23$, the critical values of correlation coefficient at $\alpha = 0.05$ and $\alpha = 0.01$ are 0.41 and 0.53, respectively. The label "-CHEM" is short for MIROC-ESM-CHEM.

IPSL-CM5A-LR/MR, IPSL-CM5B-LR, MIROC-ESM, MIROC-ESM-CHEM, and MPI-ESM-MR) are less than half of that given by P2010.

Table 3 also shows that the model SD of interannual variation between 15° and 80°N is close to the result of 0.04 given by P2010. Between 15° and 80°S, the models have more discrepancies from P2010. The observationally based results of P2010 show that the strong variability over the Southern Ocean south of 45°S is smaller than or similar to the variability over the tropical Pacific. However, in most of the CMIP5 models, the SD of the interannual variability over the Southern Ocean is much bigger than that over the tropical Pacific (e.g., in HadGEM2-CC/ES, IPSL-CM5A-LR/MR, MIROC-ESM, MIROC-ESM-CHEM, and MPI-ESM-LR/MR). Between

15° and 80°S, 14 of the 18 models have bigger SD values than that of P2010, and they are BCC_CSM1.1, CanESM2, CESM1(BGC), GFDL-ESM2G/M, HadGEM2-CC/ ES, IPSL-CM5A/B-LR, MIROC-ESM, MIROC-ESM-CHEM, MPI-ESM-LR/MR, and NorESM1-ME.

Figure 5 shows the time series of air–sea $CO_2$ flux anomalies in different regions (global, 15°–80°N, 15°–80°S, and tropical Pacific of 15°S–15°N, 109°E–77°W). The CCs between these regions are shown above each panel in Fig. 5. In P2010, the CCs between the global air–sea $CO_2$ flux anomalies and the anomalies over each of the other three areas are between 0.72 and 0.88, all passing a Student's $t$ test at the significance level of 95%. The CC between the tropical Pacific of 15°S–15°N and the global ocean is the highest (CC = 0.88) in P2010.
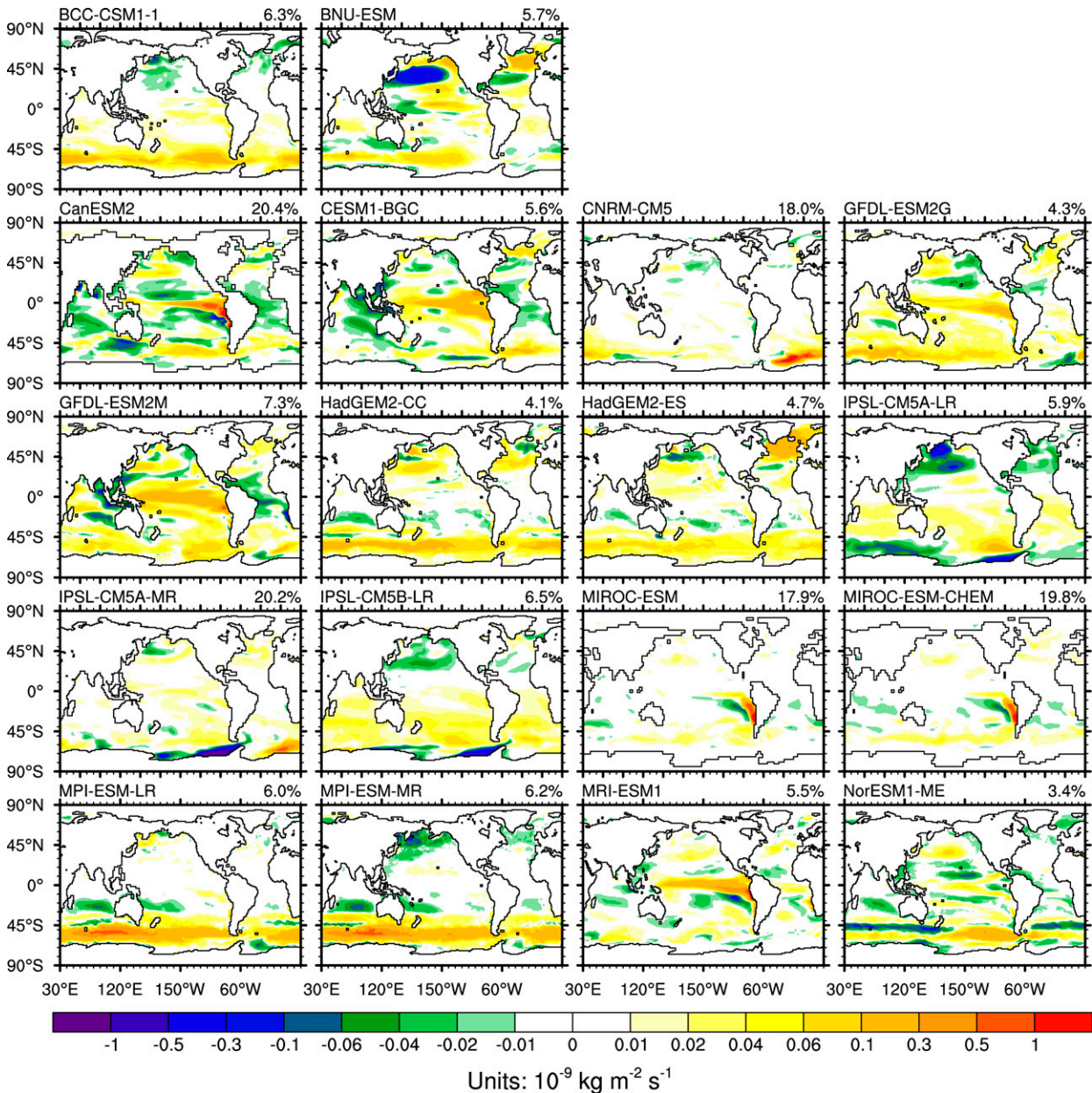
FIG. 6. EOF1 of model air–sea $CO_2$ flux ($10^{-9}$ kg m$^{-2}$ s$^{-1}$) over the global ocean during 1870–2000. Variance explained by each mode is given at the top right of each panel. EOFs are based on monthly data. To show the variation better, we use a nonlinear color scaling.

However, this high correlation is missing in most CMIP5 models. The air–sea $CO_2$ flux anomalies in the global ocean in most CMIP5 models are consistent with the anomalies between 15° and 80°S, rather than with those in the tropical Pacific. In most CMIP5 models, the Southern Ocean around 60°S represents a carbon sink or a weak carbon source, which is different from the observation-based results. These biases from the annual mean would make it difficult to trust the responses of the Southern Ocean to climate change in CMIP5 models. In

the following subsection, we investigate the variation of air–sea $CO_2$ flux through EOF decomposition.

### b. Spatial distribution variation during 1870–2000 over the global ocean

The $CO_2$ flux variability over the central-eastern tropical Pacific associated with the ENSO cycle dominates the global interannual variability (McKinley et al. 2004a,b; P2010; Rödenbeck et al. 2014). The EOF1 of air–sea $CO_2$ flux displays the ENSO mode (McKinley
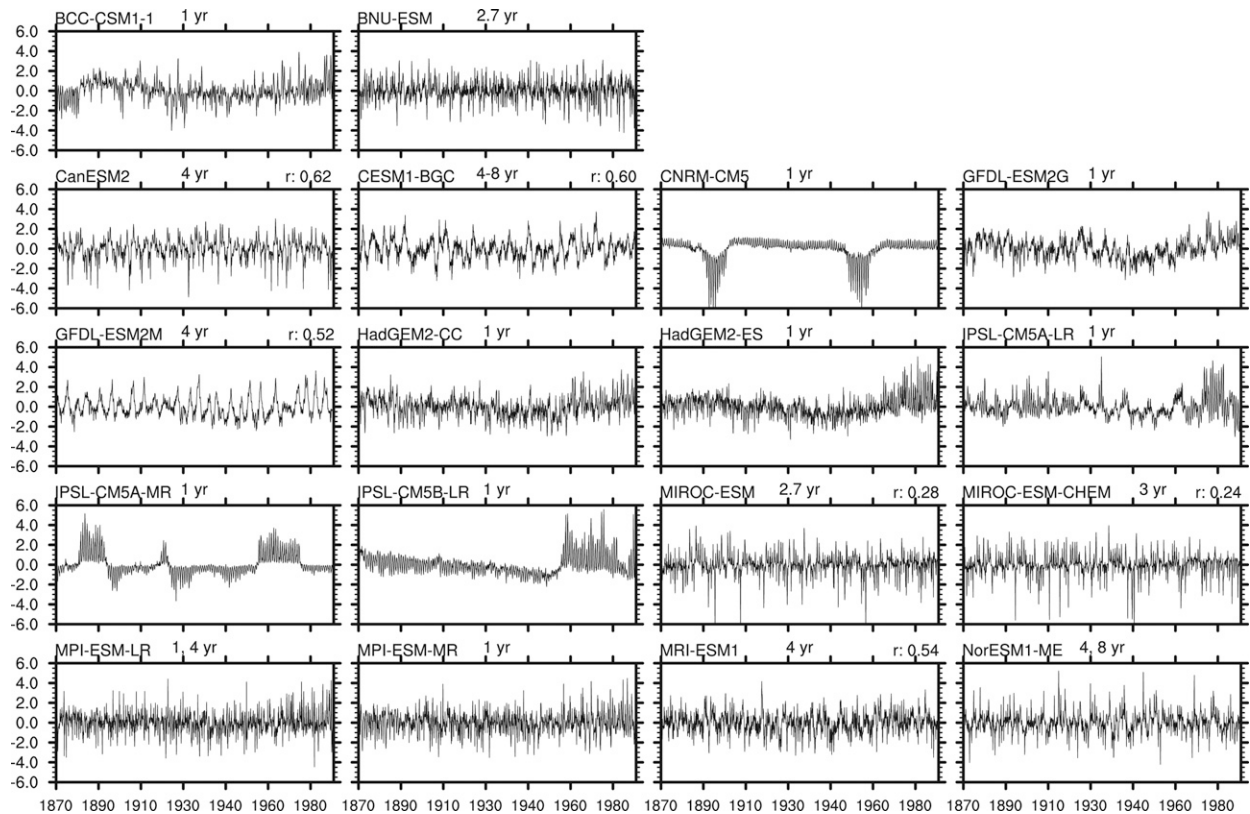
FIG. 7. PC1 of air–sea $CO_2$ flux over the global ocean during 1870–2000. The number in the middle above each panel is the main period of PC1. The number on the right above selected panels is the correlation coefficient between PC1 and ENSO index.

et al. 2004b; Fig. S5 in the supplemental material). Here, we examine spatial features of interannual variation of air–sea $CO_2$ flux in the 18 models using a longer period from 1870 to 2000 and using EOF analysis over the global ocean.

Figure 6 shows the EOF1 of model air–sea $CO_2$ flux over the global ocean, and Fig. 7 is the corresponding PC1. Observationally based results show that the transport of seawater enriched with DIC over the tropical Pacific to the surface ocean is constrained during El Niño events (with positive SST anomalies over the central-eastern tropical Pacific) because of the weakening of equatorial upwelling, which in turn influences $pCO_2$ in seawater and dominates the variation of air–sea $CO_2$ flux ultimately (Feely et al. 2002). However, only seven models [CanESM2, CESM1(BGC), GFDL-ESM2G/M, MIROC-ESM, MIROC-ESM-CHEM, and MRI-ESM1] capture the EOF1 signal with strong fluctuations in the tropical Pacific (Fig. 6), as pointed out in previous studies of Le Quéré et al. (2000), McKinley et al. (2004a,b), and Li and Xu (2013). The strongest fluctuation of air–sea $CO_2$ flux in most models happens in the Southern Ocean (BCC_CSM1.1, BNU-ESM, HadGEM2-CC/ES, MPI-ESM-LR/MR, and NorESM1-ME) or in the high latitudes

of the Northern Hemisphere (BNU-ESM, CNRM-CM4, and HadGEM2-CC/ES), which coincides with the SD fluctuation shown in Fig. 4.

The EOF1 of global SST in the models illustrates strong fluctuations in the tropical Pacific (Fig. S6 in the supplemental material). The associated PC1 is correlated with the ENSO index, which is defined as the area-mean SST anomalies in the region of 5°S–5°N, 120°–170°W, with CCs ranging from 0.83 to 0.96 (Table 4; the number on the right above each panel in Fig. S7 of the supplemental material). This means the EOF1 of SST in the CMIP5 models is the ENSO mode. Because of reduced upwelling of DIC-rich deep water to the surface during El Niño events, the tropical Pacific exports less $CO_2$ during an El Niño event than in a normal year (Li and Xu 2013; Landschützer et al. 2014; Rödenbeck et al. 2014); thus, the air–sea $CO_2$ flux anomalies and SST anomalies have positive correlation (for $CO_2$ into the ocean, the flux is positive). To examine why the models are poor in presenting the ENSO mode of air–sea $CO_2$ flux over the global ocean, we conduct power spectral analysis on PC1 of global air–sea $CO_2$ flux and on the ENSO index, respectively, focusing on their main periods (power spectra not shown) and their CCs. Here, we define the period

TABLE 4. Correlation coefficients between $PC1_{SST}$ and ENSO index over the global ocean; between $PC1_{CO_2}$ and $PC1_{SST}$ over the global ocean (G) and the tropical Pacific (TP; 15°S–15°N, 109°E–77°W); between $PC1_{CO_2}$ and ENSO index over G and TP; and main periods of ENSO events, $PC1_{CO_2}$, and $PC1_{SST}$ during 1870–2000. If the model is capable of displaying the ENSO mode of air–sea $CO_2$ flux, it is marked with Y, and N means the opposite. The period of ENSO events is presented by the period of ENSO index. The ENSO index is defined as the area-mean SST anomalies in the region of 5°S–5°N, 120°–170°W. When $n = 1572$, the critical values of correlation coefficient at $\alpha = 0.05$ and $\alpha = 0.01$ are 0.049 and 0.065, respectively.

| Models | Main periods of ENSO events (yr) | CCs between $PC1_{SST}$ and ENSO index | Main periods of $PC1_{CO_2}$ (yr) | | CCs between $PC1_{CO_2}$ and $PC1_{SST}$ | | CCs between $PC1_{CO_2}$ and ENSO index | | ENSO mode in EOF1 of air–sea $CO_2$ flux | |
| | | G | G | TP | G | TP | G | TP | G | TP |
|---|---|---|---|---|---|---|---|---|---|---|
| BCC_CSM1.1 | 2.7 | 0.83 | 1 | 2.7 | 0.05 | 0.60 | −0.04 | 0.60 | N | Y |
| BNU-ESM | 3.3 and 2 | 0.89 | 2.7 | 2.7 | −0.38 | −0.37 | −0.26 | −0.22 | N | N |
| CanESM2 | 4 | 0.92 | 4 | 4 | 0.62 | 0.71 | 0.62 | 0.67 | Y | Y |
| CESM1(BGC) | 2–4 | 0.95 | 4–8 | 4–8 | 0.73 | 0.59 | 0.60 | 0.55 | Y | Y |
| CNRM-CM5 | 4 | 0.94 | 1 | 2 | 0.05 | 0.05 | 0.04 | −0.28 | N | N |
| GFDL-ESM2G | 3–4 | 0.88 | 1 | 4–5 | 0.55 | 0.66 | 0.39 | 0.58 | N | Y |
| GFDL-ESM2M | 4.7 | 0.96 | 4 | 4 | 0.67 | 0.64 | 0.52 | 0.54 | Y | Y |
| HadGEM2-CC | 5 | 0.90 | 1 | 1 | 0.29 | −0.33 | 0.20 | −0.36 | N | N |
| HadGEM2-ES | 2–2.5 | 0.91 | 1 | 1 | 0.10 | −0.25 | 0.02 | −0.25 | N | N |
| IPSL-CM5A-LR | 2–4 | 0.88 | 1 | 4 | −0.24 | 0.73 | −0.19 | 0.25 | N | Y |
| IPSL-CM5A-MR | 4 | 0.91 | 1 | 4 | 0.09 | 0.79 | −0.01 | 0.74 | N | Y |
| IPSL-CM5B-LR | 2–4 | 0.92 | 1 | 4 | −0.02 | 0.70 | −0.02 | 0.13 | N | Y |
| MIROC-ESM | 4 | 0.84 | 2.7 | 1 | 0.32 | 0.55 | 0.28 | 0.45 | Y | Y |
| MIROC-ESM-CHEM | 3–4 | 0.89 | 3 | 1.2 | 0.30 | 0.51 | 0.24 | 0.44 | Y | Y |
| MPI-ESM-LR | 4–8 | 0.91 | 1 and 4 | 1 | 0.16 | 0.16 | 0.11 | 0.07 | N | N |
| MPI-ESM-MR | 4–5 | 0.89 | 1 | 1 | 0.20 | 0.19 | 0.11 | −0.25 | N | N |
| MRI-ESM1 | 4 | 0.85 | 4 | 4 | 0.50 | 0.64 | 0.54 | 0.60 | Y | Y |
| NorESM1-ME | 2–4 and 8 | 0.96 | 4 and 8 | 4 | 0.53 | −0.31 | 0.46 | −0.32 | N | N |

corresponding to the highest spectral density and passing the 95% significance level as the main period. The results are shown in Table 4.

The ENSO period indicated by the main period of the ENSO index is 2–8 yr in the 18 CMIP5 models, which is close to the observed ENSO period. For the main period of PC1 of air–sea $CO_2$ flux ($PC1_{CO_2}$), as listed in Table 4, except for GFDL-ESM2G, the other six of the seven models that capture the EOF1 signal with large fluctuations in the tropical Pacific also show the period of $PC1_{CO_2}$ similar to the observed period of ENSO events. The CCs between the global air–sea $CO_2$ flux's PC1 and ENSO index in these six models are between 0.30 and 0.68 (Table 4; the number on the right above the panels in Fig. 7), which illustrates that the EOF1 of the global air–sea $CO_2$ flux is the ENSO mode. GFDL-ESM2G captures the EOF1 signal with large fluctuations in the tropical Pacific, whereas the period of its $PC1_{CO_2}$ is one year and shorter than the observed ENSO period. In the remaining 11 models, the main period of $PC1_{CO_2}$ over the global ocean in 8 models is about one year or less (Table 4; the number in the middle above the panels in Fig. 7), much shorter than the period of the observed ENSO events.

In the observation, the interannual variation of global air–sea $CO_2$ flux is dominated by the variation in the tropical Pacific (Feely et al. 1997, 1999; Jones et al. 2001; Obata and Kitamura 2003; McKinley et al. 2004b; Patra et al. 2005; P2010). So we analyze the interannual variation of the tropical Pacific air–sea $CO_2$ flux in the following subsection.

### c. Spatial distribution variation during 1870–2000 over the tropical Pacific

Figure 8 shows the EOF1 of model air–sea $CO_2$ flux over the tropical Pacific (15°S–15°N, 109°E–77°W), and Fig. 9 is the corresponding PC1. The explained variances of EOF1 in Fig. 8 are strikingly different among the models, with the maximum value of 57.8% (CanESM2) and the minimum value of 9.6% (MPI-ESM-MR). The center locations of strong fluctuation in EOF1 also show large differences from model to model. For example, in BCC_CSM1.1 and IPSL-CM5B-LR, strong fluctuations mainly happen in the western Pacific warm pool, as in Landschützer et al. (2014). In GFDL-ESM2G/M and MRI-ESM1, large fluctuations happen in the whole tropical Pacific. In the other models [CanESM2, CESM1(BGC), IPSL-CM5A-LR/MR,
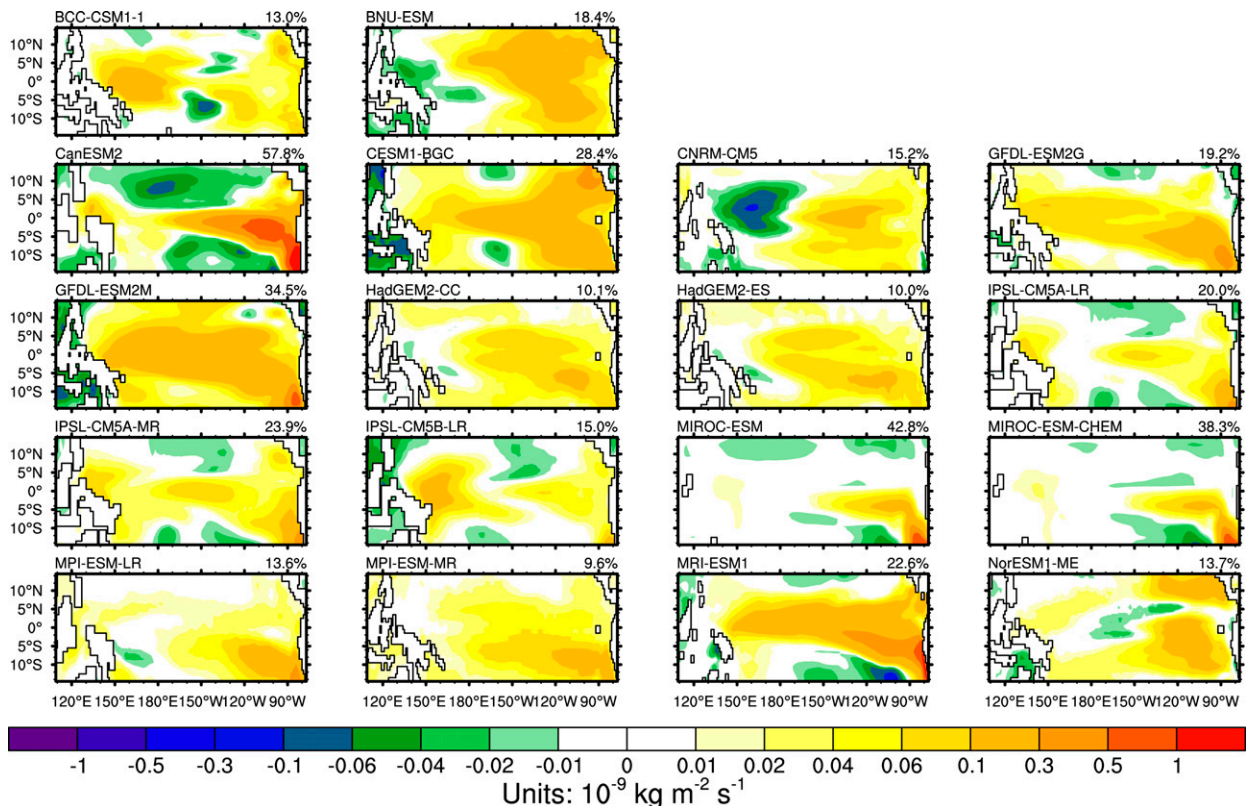
FIG. 8. As in Fig. 6, but for over the tropical Pacific (15°S–15°N, 109°E–77°W).

MIROC-ESM, and MIROC-ESM-CHEM], strong fluctuations mainly happen in the central-eastern tropical Pacific, which is consistent with some observationally based and modeling studies (McKinley et al. 2004b; P2010). In BNU-ESM and CNRM-CM5, the variation in the western tropical Pacific is out of phase with that in the central-eastern tropical Pacific, which is not consistent with any existing results.

In the 18 models, the SST anomalies in the tropical Pacific all clearly show the ENSO mode [e.g., observed ENSO periods and close CCs between PC1 of SST ($PC1_{SST}$) and ENSO index; Figs. 10 and 11]. In the six models capable of representing the ENSO mode of air–sea $CO_2$ flux over the global ocean, the DIC anomalies between 15°S–15°N also fluctuate with the alternating warm/cold SST anomalies but are out of phase (except for MIROC-ESM and MIROC-ESM-CHEM, which do not provide DIC data; not shown). For the models failing to display the ENSO mode of air–sea $CO_2$ flux over the global ocean, except for BCC_CSM1.1 and BNU-ESM that do not provide DIC data, four of them are capable of showing the out-of-phase fluctuation of DIC anomalies with the SST anomalies in the tropical Pacific (GFDL-ESM2G, IPSL-CM5A-LR/MR, and IPSL-CM5B-LR), with the CCs between SST anomalies and DIC anomalies

being about −0.60 (in GFDL-ESM2G) and −0.65 (in the three models of IPSL), and their period of $PC1_{CO_2}$ over the tropical Pacific (Table 4; the number in the middle above the panels in Fig. 9) is similar to the observed period of ENSO events. There is another model (CNRM-CM5), which has the normal period of $PC1_{CO_2}$ over the tropical Pacific, but the relation between SST anomalies and DIC anomalies is weak (CC = −0.08). There are four models (HadGEM2-CC/ES and MPI-ESM-LR/MR) that show strong negative relations between SST anomalies and DIC anomalies with the CCs between −0.33 and −0.56; their period of $PC1_{CO_2}$ over the tropical Pacific is one year, which is much shorter than the observed ENSO period. In addition, the CCs between $PC1_{CO_2}$ and the time series corresponding to $PC1_{SST}$ in HadGEM2-CC/ES are negative, and those in MPI-ESM-LR/MR are smaller than those in the other models (Table 4). This means that these models may not have the correct mechanism(s) of interannual variation in the tropical Pacific, despite showing close relationships between SST anomalies and DIC anomalies. The eight models that have observed ENSO period of $PC1_{CO_2}$ are examined further.

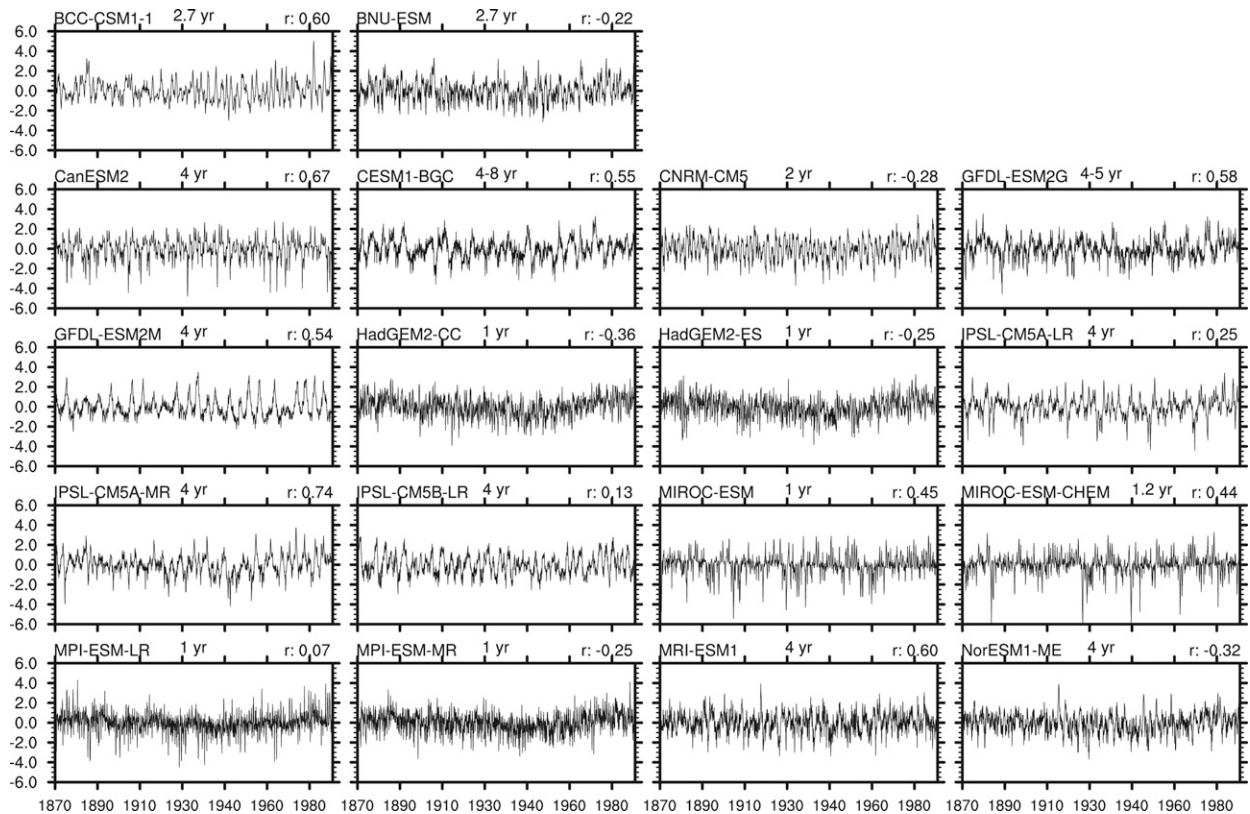Over the tropical Pacific, the five models BCC_CSM1.1, GFDL-ESM2G, IPSL-CM5A-LR/MR, and IPSL-CM5B-LR

FIG. 9. As in Fig. 7, but for over the tropical Pacific (15°S–15°N, 109°E–77°W). The number on the right above each panel is the correlation coefficient between PC1 and ENSO index.

have similar EOF1 modes of SST and air–sea $CO_2$ flux (Figs. 8 and 10); their positive correlations between $PC1_{CO_2}$ and the ENSO index range from 0.13 to 0.74 (Table 4; Fig. 9), and their positive correlations between $PC1_{CO_2}$ and $PC1_{SST}$ range from 0.60 to 0.79 (Table 4). Similar EOF1 patterns and positive correlations show the four models' capability of representing the ENSO mode as well as in-phase fluctuations of air–sea $CO_2$ flux and SST in the central-eastern tropical Pacific. In the five models BCC_CSM1.1, GFDL-ESM2G, IPSL-CM5A-LR/MR, and IPSL-CM5B-LR, the air–sea $CO_2$ flux fluctuations are in the central-eastern tropical Pacific as well as in the western Pacific warm pool (Fig. 8), and the fluctuations in these two regions are in phase. During El Niño events, the eastern tropical Pacific shows reduced air–sea $CO_2$ flux mainly because of reduced equatorial upwelling of DIC-rich deep water; the western tropical Pacific also shows reduced air–sea $CO_2$ flux because of the cold anomalies in SST. In the five models, the failure to reproduce the dominating role of the tropical Pacific in the interannual variation of global air–sea $CO_2$ flux can be attributed to the much stronger variability in the high latitudes of the Southern Hemisphere.

There is another kind of model: for example, BNU-ESM and CNRM-CM5. In these two models, the air–sea

$CO_2$ flux over the western tropical Pacific shows an out-of-phase fluctuation with that in the eastern tropical Pacific (Fig. 8). Negative CCs between air–sea $CO_2$ flux anomalies and SST anomalies, between air–sea $CO_2$ flux anomalies and ENSO index, and between $PC1_{CO_2}$ and ENSO index (all passing a Student's $t$ test at the significance level of 95%) show the influence of $CO_2$ solubility on the air–sea $CO_2$ flux controlled by SST instead of the dominating role of DIC on the air–sea $CO_2$ flux controlled by upwelling. In these two models, during El Niño events, the role of warmer SST anomalies in $CO_2$ solubility becomes outstanding in terms of increasing $CO_2$ outgassing over the central-eastern tropical Pacific. In contrast, the colder SST anomalies over the western tropical Pacific warm pool help to reduce $CO_2$ outgassing there.

The remaining model (NorESM1-ME) also shows fluctuations of air–sea $CO_2$ flux in the tropical Pacific (Fig. 8), but the CC between its PC1 of air–sea $CO_2$ flux and that of the ENSO index is negative, although the CC between the SST anomalies and DIC anomalies is up to $-0.38$.

As a summary, except for the six models that represent the ENSO mode of the air–sea $CO_2$ flux both over the global ocean and the tropical Pacific, the results of the
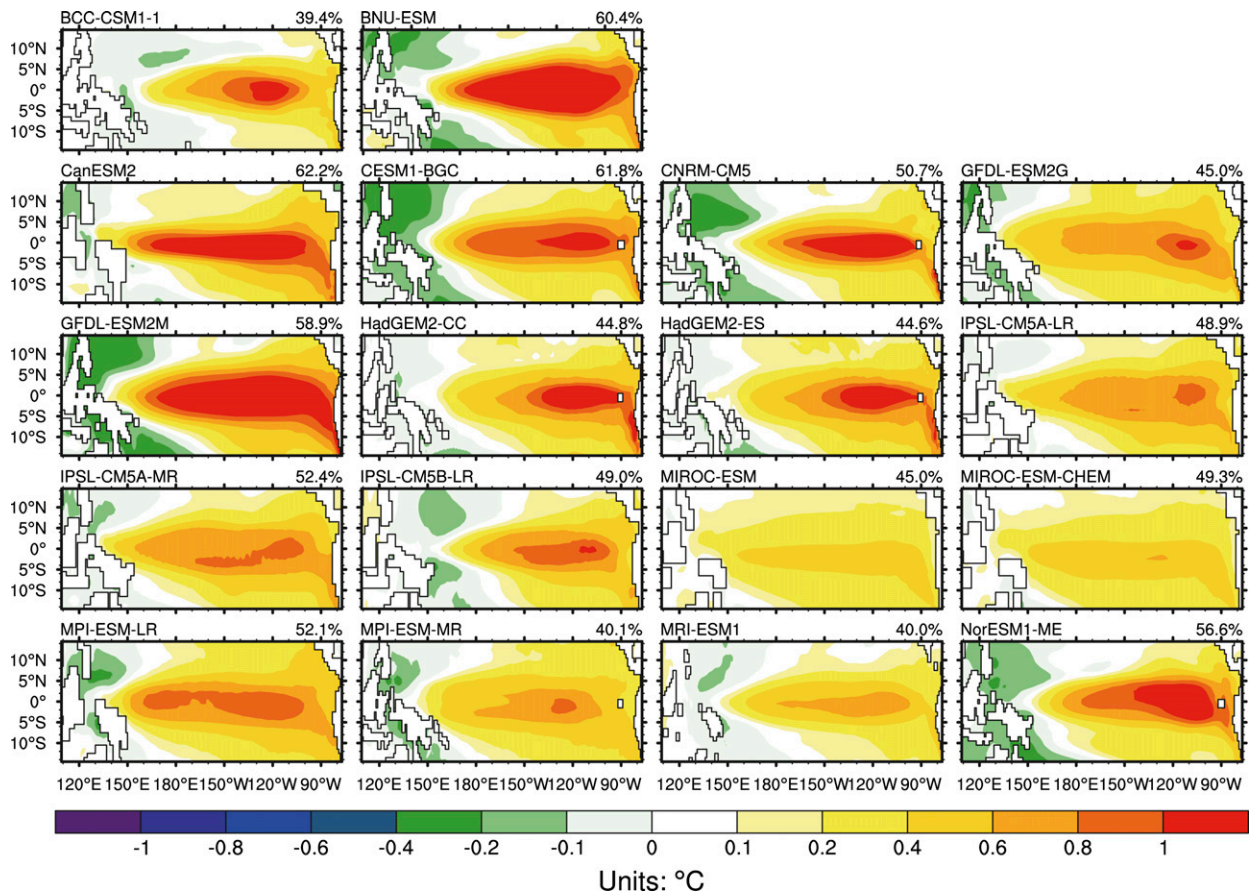
FIG. 10. EOF1 of model SST (°C) over the tropical Pacific (15°S–15°N, 109°E–77°W) during 1870–2000. Variance explained by each mode is given at the top right of each panel. EOFs are based on monthly data. To show the variation better, we use a nonlinear color scaling.

remaining 12 models are as follows. The EOF1 mode of air–sea $CO_2$ flux in BCC_CSM1.1, GFDL-ESM2G, and the three models of IPSL describes the ENSO mode over the tropical Pacific. BNU-ESM and CNRM-CM5 have a similar period for the observed ENSO period but have wrong mechanism(s) of the interannual variability of air–sea $CO_2$ flux. In the four models HadGEM2-CC/ES and MPI-ESM-LR/MR, the periods of air–sea $CO_2$ flux are not in the range of the observed ENSO periods, although their relations between SST anomalies and DIC anomalies are reasonable.

## 5. Summary and discussion

### a. Differences in air–sea $CO_2$ flux parameterizations

The air–sea $CO_2$ flux in the CMIP5 models is computed as the product of sea–air $pCO_2$ difference, the solubility of $CO_2$ in seawater, and air–sea gas transfer velocity. Most of the CMIP5 models adopt the same parameterization of air–sea gas transfer rate, which is a function of wind speed (Takahashi et al. 2009), and the same formula

for $CO_2$ solubility. Simulated surface seawater DIC (and hence $pCO_2$) values among these models also differ because of different physical and biogeochemical processes in these models. Therefore, under the same prescribed atmospheric $CO_2$ forcing in the historical experiment (Taylor et al. 2012), simulated air–sea $CO_2$ fluxes among these models can be quite different.

### b. Model air–sea $CO_2$ flux biases and their underlying causes

For the period of 1996–2004, the CMIP5 models perform well in terms of multiyear mean of air–sea $CO_2$ flux, except for the two models CMCC-CESM and INM-CM4.0, which show low SCCs and high RMSEs with respect to the observationally based results of VM2010, and for the two models GISS-E2-H/R-CC, which underestimate the annual mean flux after the Industrial Revolution. More than half of the remaining 18 models capture the distribution of air–sea $CO_2$ flux reasonably well, with higher SCCs and lower RMSEs compared
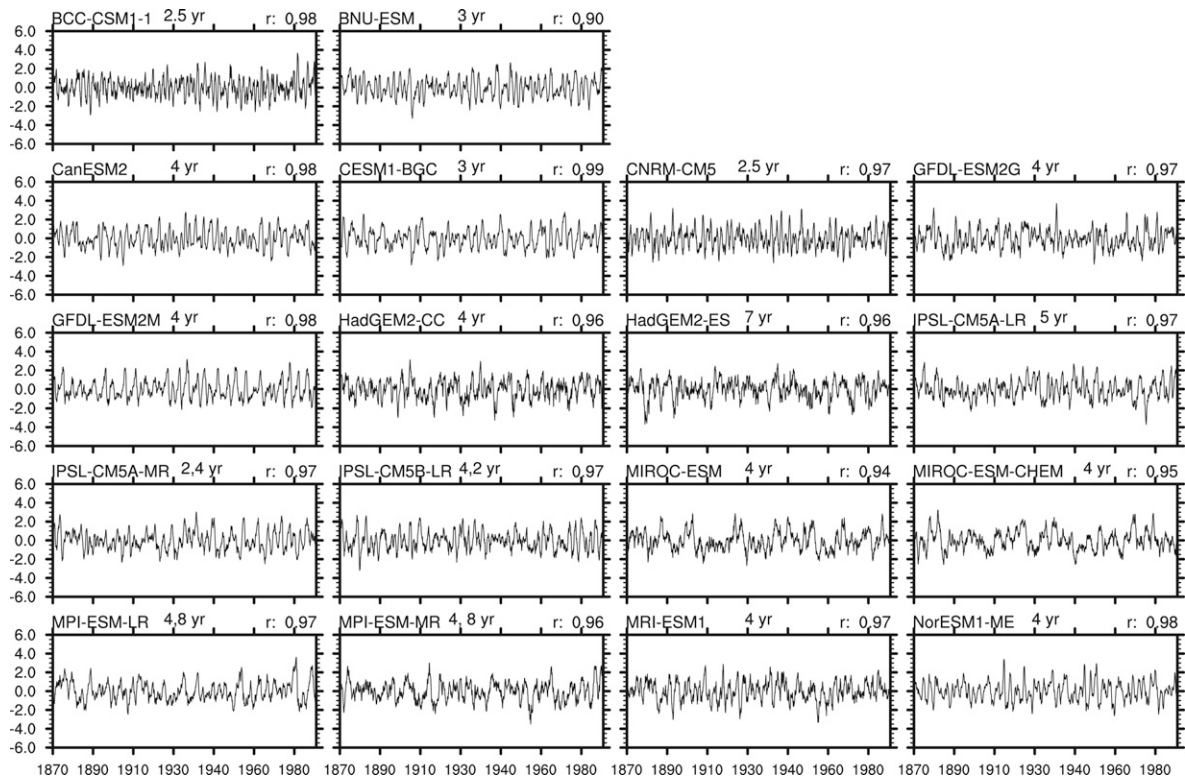
FIG. 11. PC1 of SST over the tropical Pacific (15°S–15°N, 109°E–77°W) during 1870–2000. The number in the middle above each panel is the period of PC1. The number on the right above each panel is the correlation coefficient between PC1 and ENSO index.

with the MME mean results of the 18 models. The MME mean shows the region south of 50°S has small annual mean flux and large annual mean increasing rate over time. How to better depict the Southern Ocean, which is a complex dynamic system and lacks observational data, is important for improving the simulation of global air–sea $CO_2$ flux.

Comparison with the observationally based results of VM2010 shows that the model flux biases are mainly concentrated in the areas of the North Atlantic, the northwestern Pacific, and around 60°S. Note that the regions where the models have biases against observations are also where the models differ most among themselves in terms of air–sea $CO_2$ flux.

In the northwestern Pacific, most models show stronger $CO_2$ uptake for different reasons, which is induced by colder SST or weaker convection in the Bering Sea. In the North Atlantic, the reduction in $CO_2$ uptake caused by underestimated intpp and weaker AMOC may exceed the increased $CO_2$ solubility induced by colder SST biases, which contributes to the weaker $CO_2$ uptake in the North Atlantic. In the Southern Ocean, most models show carbon sinks there, which is not consistent with the observationally based results of VM2010, or have weaker $CO_2$ outgassing in the open ocean around 60°S. On the one hand, the simulated

strengthening of the bottom-water formation (Heuzé et al. 2013) and the reduction of the SIE (Turner et al. 2013) would promote $CO_2$ uptake by the ocean. On the other hand, compared with the results of satellite product, the models have clearly overestimated intpp. Improvements in the AMOC, Southern Ocean bottom-water formation, and the SIE in the Antarctic may help reduce the errors in air–sea $CO_2$ flux in the models.

It should be noted that, although the models share some simulation biases of air–sea $CO_2$ flux, the causes underlying their similar biases may be different. For example, in the northwestern Pacific, in those models having underestimated intpp compared with the satellite product of intpp (e.g., CanESM2, CNRM-CM5, GISS-E2-H/R-CC, IPSL-CM5A-LR/MR, IPSL-CM5B-LR, and MRI-ESM1), the stronger $CO_2$ uptake more likely stems from physical drivers (e.g., cold SST in the models; Fig. S2). In GFDL-ESM2G and MPI-ESM-LR/MR, the colder SST and overestimated biological effects represented by intpp jointly contribute to stronger $CO_2$ uptake. We hope that the sources of biases could be quantified better when more outputs become available, including both physical and biological fields (e.g., the concentration of DIC at different ocean
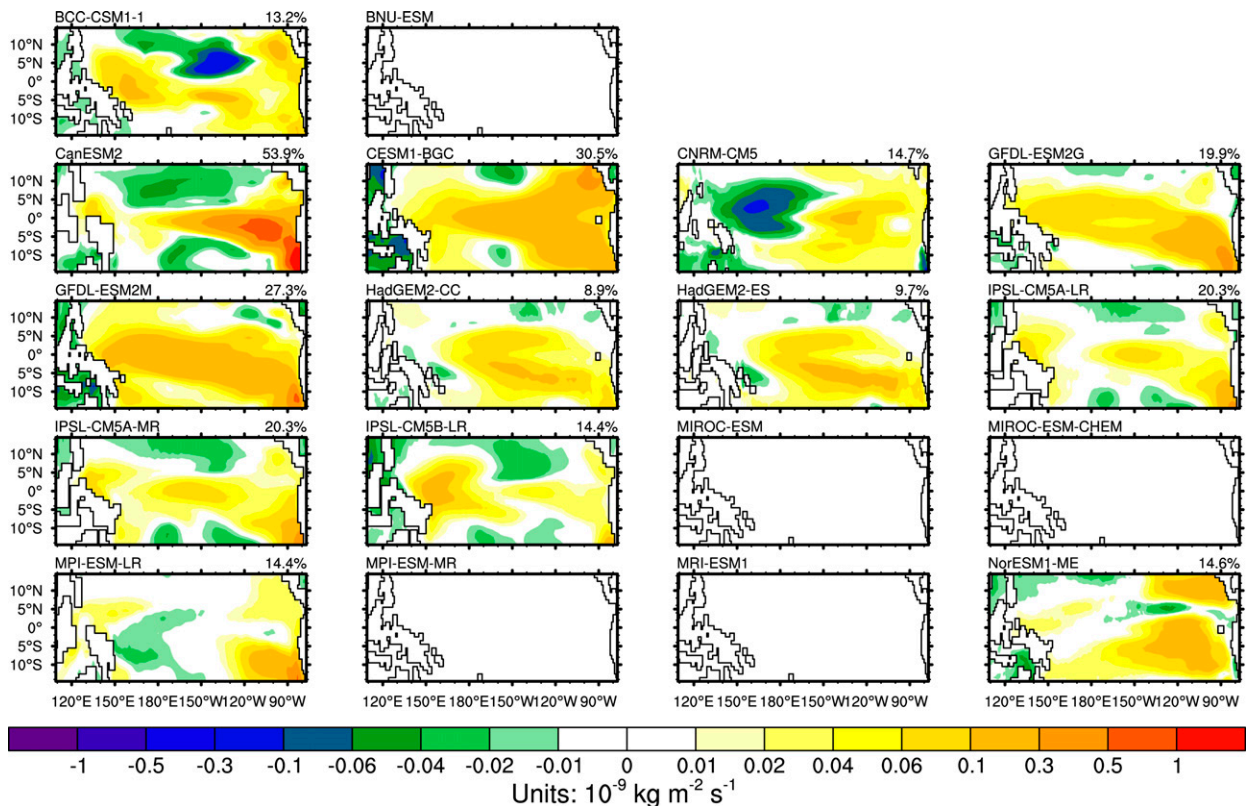
FIG. 12. EOF1 of model air–sea $CO_2$ flux ($10^{-9}$ kg m$^{-2}$ s$^{-1}$) over the tropical Pacific (15°S–15°N, 109°E–77°W) during the last 131 yr (corresponding to the time period of 1870–2000 in Fig. 8) of the piControl experiment. Variance explained by each mode is given at the top right of each panel. EOFs are based on monthly data. To show the variation better, we use a nonlinear color scaling. A panel with no data means the model output is not available.

depths). In addition, more realizations of a single model may help us better understand the biases in that particular model.

### c. Interannual variation of air–sea $CO_2$ flux and ENSO events

The air–sea $CO_2$ flux variations in both the tropical Pacific and global ocean are dominated by ENSO events (Feely et al. 2002; McKinley et al. 2003; P2010; Ishii et al. 2014; Landschützer et al. 2014; Rödenbeck et al. 2014). During an El Niño event, transport of DIC-rich deep water to the surface ocean is reduced because of weakened upwelling over the central-eastern tropical Pacific (Feely et al. 2002; McKinley et al. 2004b; Li and Xu 2013), which is the dominant cause of the reduction of $CO_2$ outgassing over the tropical Pacific. The opposite occurs during a La Niña event. If these mechanisms are not well represented, the model may be limited in showing the responses of air–sea $CO_2$ flux to El Niño events and in simulating air–sea $CO_2$ flux interannual variation.

Our study shows that in the 18 CMIP5 models (excluding the 4 models with poor performances, i.e.,

CMCC-CESM, GISS-E2-H/R-CC, and INM-CM4.0), 6 models [CanESM2, CESM1(BGC), GFDL-ESM2M, MIROC-ESM, MIROC-ESM-CHEM, and MRI-ESM1] are capable of capturing the ENSO mode of air–sea $CO_2$ flux in both the global ocean and tropical Pacific. CESM1(BCG) has the most similar EOF1 of the air–sea $CO_2$ flux to previous model results (McKinley et al. 2004b) and the observationally based result of P2010 (Fig. S5). In each of the six models, the distribution of strong air–sea $CO_2$ flux variation over the tropical Pacific is similar to the ENSO pattern of the global air–sea $CO_2$ flux (Figs. 6 and 8), which implies the dominating role of ENSO events in driving the interannual variability of air–sea $CO_2$ flux.

In the remaining 12 models, 5 models (BCC_CSM1.1, GFDL-ESM2G, IPSL-CM5A-LR/MR, and IPSL-CM5B-LR) are able to describe the ENSO mode of air–sea $CO_2$ flux over the topical Pacific. However, the interannual variability of the air–sea $CO_2$ flux over 15°–80°S in these models is larger than that over 15°S–15°N, which may be the reason why the tropical Pacific loses its dominating role in determining the global air–sea $CO_2$ flux variation in these models.
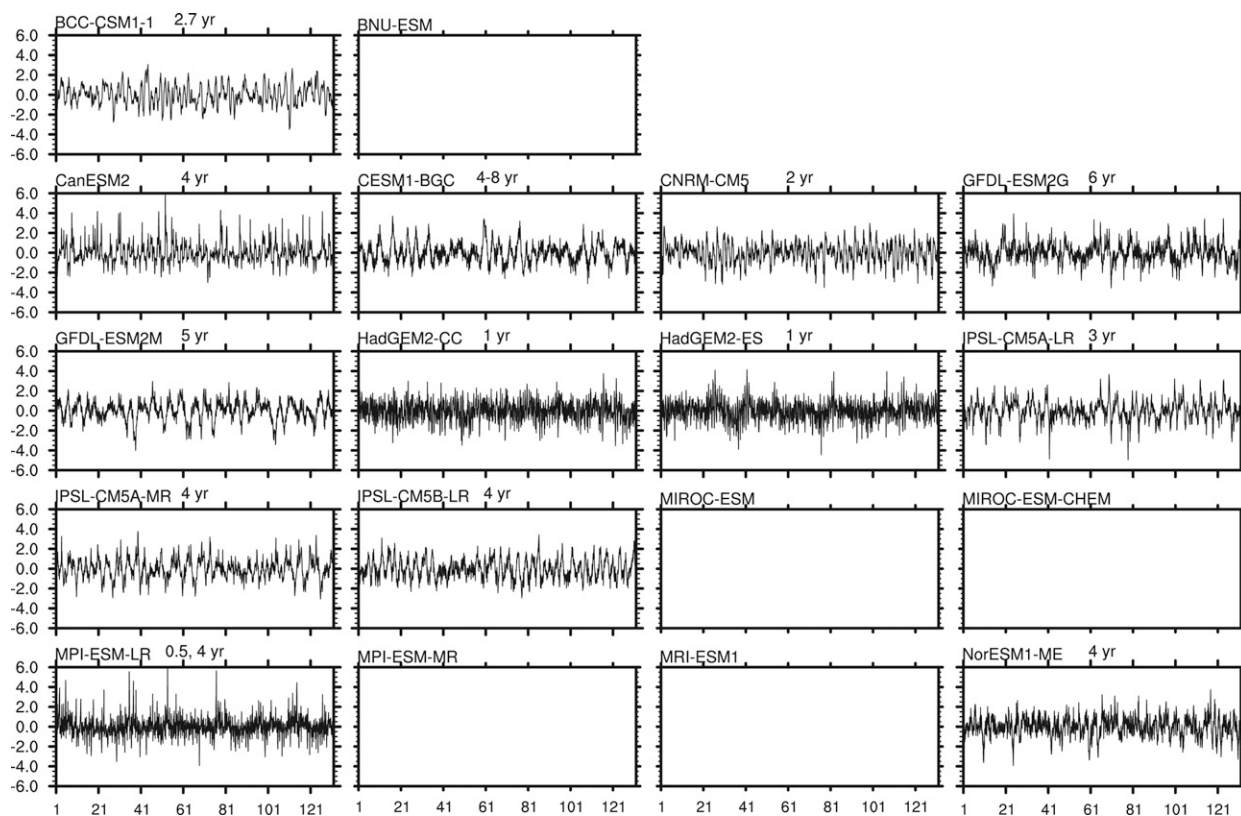
FIG. 13. PC1 of air–sea $CO_2$ flux over the tropical Pacific (15°S–15°N, 109°E–77°W) during the last 131 yr (corresponding to the time period of 1870–2000 in Fig. 9) of the piControl experiment. The number in the middle above panels is the period of PC1. A panel with no data means the model output is not available.

The other six models (not including NorESM1-ME) have less skill at representing the interannual variation of air–sea $CO_2$ flux over the tropical Pacific in two different ways. BNU-ESM and CNRM-CM5 have a similar period of air–sea $CO_2$ flux as the observed ENSO period but show incorrect relationships between SST anomalies and DIC anomalies. In these two models, the air–sea $CO_2$ flux variation is dominated by $CO_2$ solubility controlled by SST anomalies over the central-eastern tropical Pacific, rather than by ENSO-induced variation in upwelling of DIC-rich deep water. The other four models (HadGEM2-CC/ES and MPI-ESM-LR/MR) have short periods of air–sea $CO_2$ flux, which are inconsistent with the period range of ENSO events, and they have poor relationships between $PC1_{CO_2}$ and $PC1_{SST}$. In HadGEM2-CC/ES, the relations between SST anomalies and DIC anomalies are reasonable over the tropical Pacific, whereas the CCs between $PC1_{CO_2}$ and $PC1_{SST}$ are negative. It can be concluded that there are other processes with shorter periods overlapping with the ENSO events, which needs to be investigated when more data (e.g., DIC at different ocean depths) become available.

The air–sea $CO_2$ flux in the historical experiment is influenced by both natural and anthropogenic changes. To distinguish the impact of different changes on the interannual variability of air–sea $CO_2$ flux, the outputs from the preindustrial control (piControl) experiment are used for comparison with those from the historical experiment. As shown in Fig. 12, the EOF1 patterns of air–sea $CO_2$ flux in the piControl experiments are similar to those in the historical experiments (Fig. 8), the PC1 values of air–sea $CO_2$ flux in the piControl experiments (Fig. 13) are similar to those in the historical experiments (Fig. 9), and the small differences between the two sets of experiments can be ignored. Except for the global and Southern Ocean $CO_2$ uptakes that have been largely unaffected by recent climate variability and change, as noted by Frölicher et al. (2015), the variations of air–sea $CO_2$ flux are not affected by the climate change associated with human activities, because the interannual air–sea $CO_2$ flux variabilities (SD, $1\sigma$) in the piControl experiments (Fig. 14) are similar to those in the historical experiments (Fig. 4). As a conclusion, the influence of anthropogenic activities on the total air–sea $CO_2$ flux in the contemporary time period is not
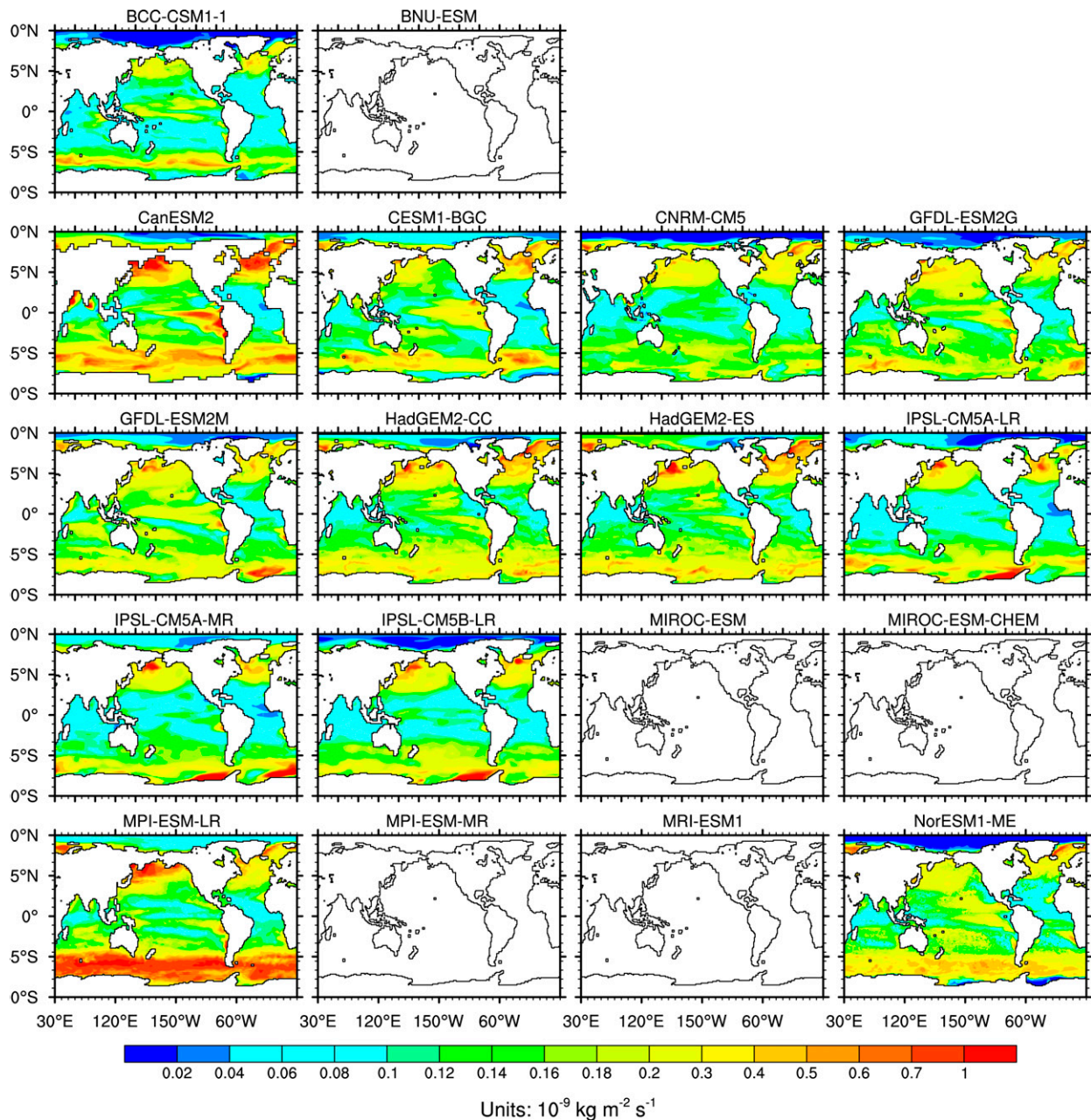
FIG. 14. Magnitude of air–sea $CO_2$ flux interannual variability ($10^{-9}$ kg m$^{-2}$ s$^{-1}$) during the last 24 yr (corresponding to the time period of 1982–2005 in Fig. 4) of the piControl experiment, which is expressed as one SD of the monthly air–sea $CO_2$ flux. The fluxes are detrended and deseasoned first. To show the variation better, we use a nonlinear color scaling. A panel with no data means the model output is not available.

obvious in these experiments. Therefore, the interannual variability of air–sea $CO_2$ flux in the CMIP5 historical simulations mainly represents features existing in natural air–sea $CO_2$ flux, which is consistent with the conclusions of Li et al. (2012).

It is noteworthy that most CMIP5 models perform better at simulating multiyear mean of air–sea $CO_2$ flux than simulating interannual variability, which indicates

there may be common issues in the representation of forcing factors closely related to the interannual variation of air–sea $CO_2$ flux in these models. The CMIP5 models' capabilities to reproduce observed air–sea $CO_2$ flux indicate the current level of the latest ESMs in simulating the ocean carbon. Our evaluation of model performances should provide useful references for model improvement and further model development.

## REFERENCES

Anav, A., and Coauthors, 2013: Evaluating the land and ocean components of the global carbon cycle in the CMIP5 Earth system models. *J. Climate*, **26**, 6801–6843, doi:10.1175/JCLI-D-12-00417.1.

Bao, Y., F. L. Qiao, and Z. Y. Song, 2012: The 3-dimensional numerical simulation of global ocean carbon cycle (in Chinese). *Acta Oceanol. Sin.*, **34**, 19–26.

Battle, M., M. L. Bender, P. P. Tans, J. White, J. T. Ellis, T. Conway, and R. J. Francey, 2000: Global carbon sinks and their variability inferred from atmospheric $O_2$ and $\delta^{13}C$. *Science*, **287**, 2467–2470, doi:10.1126/science.287.5462.2467.

Boutin, J., and J. Etcheto, 1997: Long-term variability of the air–sea $CO_2$ exchange coefficient: Consequences for the $CO_2$ fluxes in the equatorial Pacific Ocean. *Global Biogeochem. Cycles*, **11**, 453–470, doi:10.1029/97GB01367.

Crueger, T., E. Roeckner, T. Raddatz, R. Schnur, and P. Wetzel, 2008: Ocean dynamics determine the response of oceanic $CO_2$ uptake to climate change. *Climate Dyn.*, **31**, 151–168, doi:10.1007/s00382-007-0342-x.

Doney, S. C., B. Tilbrook, S. Roy, N. Metzl, C. Le Quéré, M. Hood, R. A. Feely, and D. Bakker, 2009: Surface-ocean $CO_2$ variability and vulnerability. *Deep-Sea Res. II*, **56**, 504–511, doi:10.1016/j.dsr2.2008.12.016.

——, L. Bopp, and M. C. Long, 2014: Historical and future trends in ocean climate and biogeochemistry. *Oceanography*, **27**, 108–119, doi:10.5670/oceanog.2014.14.

Dufresne, J., and Coauthors, 2013: Climate change projections using the IPSL-CM5 Earth System Model: From CMIP3 to CMIP5. *Climate Dyn.*, **40**, 2123–2165, doi:10.1007/s00382-012-1636-1.

Feely, R. A., R. Wanninkhof, C. Goyet, D. E. Archer, and T. Takahashi, 1997: Variability of $CO_2$ distributions and sea–air fluxes in the central and eastern equatorial Pacific during the 1991–1994 El Niño. *Deep-Sea Res. II*, **44**, 1851–1867, doi:10.1016/S0967-0645(97)00061-1.

——, ——, T. Takahashi, and P. Tans, 1999: Influence of El Niño on the equatorial Pacific contribution to atmospheric $CO_2$ accumulation. *Nature*, **398**, 597–601, doi:10.1038/19273.

——, C. L. Sabine, T. Takahashi, and R. Wanninkhof, 2001: Uptake and storage of carbon dioxide in the ocean: The global $CO_2$ survey. *Oceanography*, **14**, 18–32, doi:10.5670/oceanog.2001.03.

——, and Coauthors, 2002: Seasonal and interannual variability of $CO_2$ in the equatorial Pacific. *Deep-Sea Res. II*, **49**, 2443–2469, doi:10.1016/S0967-0645(02)00044-9.

——, T. Takahashi, R. Wanninkhof, M. J. McPhaden, C. E. Cosca, S. C. Sutherland, and M. E. Carr, 2006: Decadal variability of the air–sea $CO_2$ fluxes in the equatorial Pacific Ocean. *J. Geophys. Res.*, **111**, C08S90, doi:10.1029/2005JC003129.

Friedlingstein, P., and Coauthors, 2006: Climate–carbon cycle feedback analysis: Results from the $C^4MIP$ Model Intercomparison. *J. Climate*, **19**, 3337–3353, doi:10.1175/JCLI3800.1.

Frölicher, T. L., J. L. Sarmiento, D. J. Paynter, J. P. Dunne, J. P. Krasting, and M. Winton, 2015: Dominance of the Southern Ocean in anthropogenic carbon and heat uptake in CMIP5 models. *J. Climate*, **28**, 862–886, doi:10.1175/JCLI-D-14-00117.1.

Giorgetta, M. A., and Coauthors, 2013: Climate and carbon cycle changes from 1850 to 2100 in MPI-ESM simulations for the Coupled Model Intercomparison Project phase 5. *J. Adv. Model. Earth Syst.*, **5**, 572–597, doi:10.1002/jame.20038.

Gloor, M., N. Gruber, J. Sarmiento, C. L. Sabine, R. A. Feely, and C. Rödenbeck, 2003: A first estimate of present and pre-industrial air–sea $CO_2$ flux patterns based on ocean interior carbon measurements and models. *Geophys. Res. Lett.*, **30**, 10–11, doi:10.1029/2002GL015594.

Gruber, N., and Coauthors, 2009: Oceanic sources, sinks, and transport of atmospheric $CO_2$. *Global Biogeochem. Cycles*, **23**, GB1005, doi:10.1029/2008GB003349.

Heuzé, C., K. J. Heywood, D. P. Stevens, and J. K. Ridley, 2013: Southern Ocean bottom water characteristics in CMIP5 models. *Geophys. Res. Lett.*, **40**, 1409–1414, doi:10.1002/grl.50287.

Hurrell, J. W., J. J. Hack, D. Shea, J. M. Caron, and J. Rosinski, 2008: A new sea surface temperature and sea ice boundary dataset for the Community Atmosphere Model. *J. Climate*, **21**, 5145–5153, doi:10.1175/2008JCLI2292.1.

Ishii, M., and Coauthors, 2014: Air–sea $CO_2$ flux in the Pacific Ocean for the period 1990–2009. *Biogeosciences*, **11**, 709–734, doi:10.5194/bg-11-709-2014.

Jones, C. D., M. Collins, P. M. Cox, and S. A. Spall, 2001: The carbon cycle response to ENSO: A coupled climate–carbon cycle model study. *J. Climate*, **14**, 4113–4129, doi:10.1175/1520-0442(2001)014<4113:TCCRTE>2.0.CO;2.

Keeling, C. D., and R. Revelle, 1985: Effects of El Niño/Southern Oscillation on the atmospheric content of carbon dioxide. *Meteoritics*, **20**, 437–450.

Key, R. M., and Coauthors, 2004: A global ocean carbon climatology: Results from Global Data Analysis Project (GLODAP). *Global Biogeochem. Cycles*, **18**, GB4031, doi:10.1029/2004GB002247.

Landschützer, P., N. Gruber, D. Bakker, and U. Schuster, 2014: Recent variability of the global ocean carbon sink. *Global Biogeochem. Cycles*, **28**, 927–949, doi:10.1002/2014GB004853.

Lenton, A., and Coauthors, 2013: Sea–air $CO_2$ fluxes in the Southern Ocean for the period 1990–2009. *Biogeosciences*, **10**, 4037–4054, doi:10.5194/bg-10-4037-2013.

Le Quéré, C., J. C. Orr, P. Monfray, O. Aumont, and G. Madec, 2000: Interannual variability of the oceanic sink of $CO_2$ from 1979 through 1997. *Global Biogeochem. Cycles*, **14**, 1247–1265, doi:10.1029/1999GB900049.

——, and Coauthors, 2009: Trends in the sources and sinks of carbon dioxide. *Nat. Geosci.*, **2**, 831–836, doi:10.1038/ngeo689.

——, T. Takahashi, E. T. Buitenhuis, C. Rödenbeck, and S. C. Sutherland, 2010: Impact of climate change and variability on the global oceanic sink of $CO_2$. *Global Biogeochem. Cycles*, **24**, GB4007, doi:10.1029/2009GB003599.

Li, Y. C., and Y. F. Xu, 2013: Interannual variations of the air–sea carbon dioxide exchange in the different regions of the Pacific Ocean. *Acta Oceanol. Sin.*, **32**, 71–79, doi:10.1007/s13131-013-0291-7.

——, ——, M. Chu, and Y. Q. Yu, 2012: Influences of climate change on the uptake and storage of anthropogenic $CO_2$ in the global ocean. *J. Meteor. Res.*, **26**, 304–317, doi:10.1007/s13351-012-0304-z.

Lutz, M. J., K. Caldeira, R. B. Dunbar, and M. J. Behrenfeld, 2007: Seasonal rhythms of net primary production and particulate organic carbon flux to depth describe the efficiency of biological pump in the global ocean. *J. Geophys. Res.*, **113**, C10011, doi:10.1029/2006JC003706.

Maier-Reimer, E., U. Mikolajewicz, and A. Winguth, 1996: Future ocean uptake of $CO_2$: Interaction between ocean circulation and biology. *Climate Dyn.*, **12**, 711–722, doi:10.1007/s003820050138.

Maksyutov, S., and Coauthors, 2012: Regional $CO_2$ flux estimates for 2009–2010 based on GOSAT and ground-based $CO_2$ observations. *Atmos. Chem. Phys. Discuss.*, **12**, 29 235–29 288, doi:10.5194/acpd-12-29235-2012.

Marinov, I., A. Gnanadesikan, J. R. Toggweiler, and J. L. Sarmiento, 2006: The Southern Ocean biogeochemical divide. *Nature*, **441**, 964–967, doi:10.1038/nature04883.

McKinley, G. A., M. J. Follows, J. Marshall, and S. M. Fan, 2003: Interannual variability of air–sea $O_2$ fluxes and the determination of $CO_2$ sinks using atmospheric $O_2/N_2$. *Geophys. Res. Lett.*, **30**, 1101, doi:10.1029/2002GL016044.

——, C. Rödenbeck, M. Gloor, S. Houweling, and M. Heimann, 2004a: Pacific dominance to global air–sea $CO_2$ flux variability: A novel atmospheric inversion agrees with ocean models. *Geophys. Res. Lett.*, **31**, L22308, doi:10.1029/2004GL021069.

——, M. J. Follows, and J. Marshall, 2004b: Mechanisms of air–sea $CO_2$ flux variability in the equatorial Pacific and the North Atlantic. *Global Biogeochem. Cycles*, **18**, GB2011, doi:10.1029/2003GB002179.

McNeil, B. I., N. Metzl, R. M. Key, R. J. Matear, and A. Corbiere, 2007: An empirical estimate of the Southern Ocean air–sea $CO_2$ flux. *Global Biogeochem. Cycles*, **21**, GB3011, doi:10.1029/2007GB002991.

Mikaloff Fletcher, S. E., and Coauthors, 2006: Inverse estimates of anthropogenic $CO_2$ uptake, transport, and storage by the ocean. *Global Biogeochem. Cycles*, **20**, GB2002, doi:10.1029/2005GB002530.

Morrison, A. K., T. L. Frölicher, and J. L. Sarmiento, 2015: Upwelling in the Southern Ocean. *Phys. Today*, **68**, 27–32, doi:10.1063/PT.3.2654.

Obata, A., 2007: Climate–carbon cycle model response to freshwater discharge into the North Atlantic. *J. Climate*, **20**, 5962–5976, doi:10.1175/2007JCLI1808.1.

——, and Y. Kitamura, 2003: Interannual variability of the sea–air exchange of $CO_2$ from 1961 to 1998 simulated with a global ocean circulation–biogeochemistry model. *J. Geophys. Res.*, **108**, 3337, doi:10.1029/2001JC001088.

Orr, J. C., and Coauthors, 2001: Estimates of anthropogenic carbon uptake from four three-dimensional global ocean models. *Global Biogeochem. Cycles*, **15**, 43–60, doi:10.1029/2000GB001273.

Park, G. H., and Coauthors, 2010: Variability of global net sea–air $CO_2$ fluxes over the last three decades using empirical relationships. *Tellus*, **62B**, 352–368, doi:10.1111/j.1600-0889.2010.00498.x.

Patra, P. K., S. Maksyutov, M. Ishizawa, T. Nakazawa, T. Takahashi, and J. Ukita, 2005: Interannual and decadal changes in the sea–air $CO_2$ flux from atmospheric $CO_2$ inverse modeling. *Global Biogeochem. Cycles*, **19**, GB4013, doi:10.1029/2004GB002257.

Rayner, N. A., D. E. Parker, E. B. Horton, C. K. Folland, L. V. Alexander, D. P. Rowell, E. C. Kent, and A. Kaplan, 2003: Global analyses of sea surface temperature, sea ice, and night marine air temperature since the late nineteenth century. *J. Geophys. Res.*, **108**, 4407, doi:10.1029/2002JD002670.

Rödenbeck, C., and Coauthors, 2014: Interannual sea–air $CO_2$ flux variability from an observation-driven ocean mixed-layer scheme. *Biogeosciences*, **11**, 4599–4613, doi:10.5194/bg-11-4599-2014.

Romanou, A., and Coauthors, 2013: Natural air–sea flux of $CO_2$ in simulations of the NASA-GISS climate model: Sensitivity to the physical ocean model formulation. *Ocean Modell.*, **66**, 26–44, doi:10.1016/j.ocemod.2013.01.008.

Sabine, C. L., and Coauthors, 2004: The oceanic sink for anthropogenic $CO_2$. *Science*, **305**, 367–371, doi:10.1126/science.1097403.

Sarmiento, J. L., P. Monfray, E. Maier Reimer, O. Aumont, R. J. Murnane, and J. C. Orr, 2000: Sea–air $CO_2$ fluxes and carbon transport: A comparison of three ocean general circulation models. *Global Biogeochem. Cycles*, **14**, 1267–1281, doi:10.1029/1999GB900062.

——, and Coauthors, 2010: Trends and regional distributions of land and ocean carbon sinks. *Biogeosciences*, **7**, 2351–2367, doi:10.5194/bg-7-2351-2010.

Sasse, T. P., B. I. McNeil, and G. Abramowitz, 2013: A new constraint on global air–sea $CO_2$ fluxes using bottle carbon data. *Geophys. Res. Lett.*, **40**, 1594–1599, doi:10.1002/grl.50342.

Schmittner, A., 2005: Decline of the marine ecosystem caused by a reduction in the Atlantic overturning circulation. *Nature*, **434**, 628–633, doi:10.1038/nature03476.

Séférian, R., D. Iudicone, L. Bopp, T. Roy, and G. Madec, 2012: Water mass analysis of effect of climate change on air–sea $CO_2$ fluxes: The Southern Ocean. *J. Climate*, **25**, 3894–3908, doi:10.1175/JCLI-D-11-00291.1.

Sweeney, C., E. Gloor, A. R. Jacobson, R. M. Key, G. McKinley, J. L. Sarmiento, and R. Wanninkhof, 2007: Constraining global air–sea gas exchange for $CO_2$ with recent bomb $^{14}C$ measurements. *Global Biogeochem. Cycles*, **21**, GB2015, doi:10.1029/2006GB002784.

Takahashi, T., R. A. Feely, R. F. Weiss, R. H. Wanninkhof, D. W. Chipman, S. C. Sutherland, and T. T. Takahashi, 1997: Global air–sea flux of $CO_2$: An estimate based on measurements of sea–air $p CO_2$ difference. *Proc. Natl. Acad. Sci. USA*, **94**, 8292–8299, doi:10.1073/pnas.94.16.8292.

——, and Coauthors, 2002: Global sea–air $CO_2$ flux based on climatological surface ocean $p CO_2$, and seasonal biological and temperature effects. *Deep-Sea Res. II*, **49**, 1601–1622, doi:10.1016/S0967-0645(02)00003-6.

——, S. C. Sutherland, and A. Kozyr, 2007: Global ocean surface water partial pressure of $CO_2$ database: Measurements performed during 1968–2006 (Version 1.0). Carbon Dioxide Information Analysis Center Tech. Rep. ORNL/CDIAC-152, NDP-08, 20 pp.

——, and Coauthors, 2009: Climatological mean and decadal change in surface ocean $p CO_2$, and net sea–air $CO_2$ flux over the global oceans. *Deep-Sea Res. II*, **56**, 554–577, doi:10.1016/j.dsr2.2008.12.009.

Taylor, K. E., R. J. Stouffer, and G. A. Meehl, 2012: An overview of CMIP5 and the experiment design. *Bull. Amer. Meteor. Soc.*, **93**, 485–498, doi:10.1175/BAMS-D-11-00094.1.

Turner, J., T. J. Bracegirdle, T. Phillips, G. J. Marshall, and J. S. Hosking, 2013: An initial assessment of Antarctic sea ice extent in the CMIP5 models. *J. Climate*, **26**, 1473–1484, doi:10.1175/JCLI-D-12-00068.1.

Valsala, V., and S. Maksyutov, 2010: Simulation and assimilation of global ocean $pCO_2$ and air–sea $CO_2$ fluxes using ship observations of surface ocean $pCO_2$ in a simplified biogeochemical offline model. *Tellus*, **62B**, 821–840, doi:10.1111/j.1600-0889.2010.00495.x.

Wang, C., L. Zhang, L. Sang-Ki, L. Wu, and R. M. Carlos, 2014: A global perspective on CMIP5 climate model biases. *Nat. Climate Change*, **4**, 201–205, doi:10.1038/nclimate2118.

Wanninkhof, R., and Coauthors, 2013: Global ocean carbon uptake: Magnitude, variability and trends. *Biogeosciences*, **10**, 1983–2000, doi:10.5194/bg-10-1983-2013.

Wetzel, P., A. Winguth, and E. Maier-Reimer, 2005: Sea-to-air $CO_2$ flux from 1948 to 2003: A model study. *Global Biogeochem. Cycles*, **19**, GB2005, doi:10.1029/2004GB002339.

Xu, Y. F., Y. F. Pu, and L. Zhao, 2005: Advances in the studies of ocean carbon-cycle model. *Adv. Earth Sci.*, **20**, 1106–1115.

Zickfeld, K., M. Eby, and A. J. Weaver, 2008: Carbon-cycle feedbacks of changes in the Atlantic meridional overturning circulation under future atmospheric $CO_2$. *Global Biogeochem. Cycles*, **22**, GB3024, doi:10.1029/2007GB003118.